An ERA5 Climatology of Synoptic-Scale Negative Potential Vorticity-Jet Interactions over the Western North Atlantic

Alexander Lojko[1], Andrew C. Winters[2], Annika Oertel[3], Christiane Jablonowski[1], and Ashley Payne[1,4]

[1]Department of Climate and Space Sciences and Engineering, University of Michigan, Ann Arbor, MI 48109, USA
[2]Department of Atmospheric and Oceanic Sciences,University of Colorado: Boulder, Boulder, CO 80309, USA
[3]Institute of Meteorology and Climate Research Troposphere Research (IMKTRO), Karlsruhe Institute of Technology, Karlsruhe, Germany
[4]Tomorrow.io, 9 Channel Center St, 7th Floor, Boston, MA 02210, USA

Correspondence: Alexander Lojko (alojko@umich.edu)

Abstract. Recent numerical modelling and theoretical work deduce that potential vorticity (PV) can turn negative in the Northern Hemisphere as a result of localized, convective heating embedded in vertical wind shear. It is further postulated that negative potential vorticity (NPV) may be relevant for the large-scale circulation as it has been observed to grow upscale into mesoscale bands when in close proximity to the jet stream, accelerating jet stream winds and degrading numerical weather prediction skill. However, these observations are largely confined to case studies. A composite investigation is proposed to evaluate whether strengthening of the jet stream is a robust response to NPV. This research focuses on synoptic-scale bands (>1650 km) of NPV that are in close proximity (<100 km) to the jet stream (NPV-jet) using ERA5 data from January 2000 – December 2021. Climatological characteristics show that NPV-jet interactions occur most frequently over the Western Atlantic (>1.2% occurrence per year at particular grid-points) during Boreal Winter along 40°N. This latitude band has also seen a 11% increase (relative-change) in NPV-jet interactions over the 22 year time-period. Separating NPV-jet interactions into distinct, large-scale flow patterns using K-means clustering illustrates the presence of a trough-ridge couplet adjacent to positive integrated vapor transport (IVT) anomalies, conducive to warm-conveyor belts and mesoscale convective systems. Even when NPV is positioned in a more adiabatic environment (i.e., far away from regions of strong IVT anomalies), robust, positive PV gradient and wind speed anomalies exist along the jet stream. Inspecting three detailed case-studies that serve as archetypes to the clusters, it is shown that the presence of NPV near the jet stream enhances wave activity flux due to NPV mutually strengthening momentum transport and the ageostrophic flux of geopotential. The results show that NPV-jet interactions can in-situ strengthen the mid-latitude jet stream and could be dynamically relevant in enhancing downstream development, despite NPV's theorized origin from sub-mesoscales.

1 Introduction

The mid-latitude jet stream is a fast flowing current of westerly air in the upper-levels of the mid-latitude troposphere. Daily variations of the jet stream wind speeds are influenced by transient eddies (Lorenz and Hartmann, 2003; Barnes et al., 2010). These eddies can take on the form of cloud diabatic heating processes, which act to perturb the jet stream's large-scale circu-

lation away from its base state (Woollings et al., 2016). Notably, the mechanisms involved in the interactions between cloud
processes and the large-scale circulation remains a significant source of theoretical uncertainty (Bony et al., 2015; Ceppi et al.,
25 2017). This uncertainty is reflected in practical applications, particularly in numerical weather prediction, where the quality
and reliability of weather forecasting models can be rapidly degraded by cloud microphysical processes interacting with the
large-scale flow (Rodwell et al., 2013; Gray et al., 2014; Grams and Archambault, 2016; Grams et al., 2018; Spreitzer et al.,
2019). Accordingly, it is crucial to further understand how cloud processes impact jet stream dynamics, both for theoretical
advancement and practical applications.

Large-scale cloud systems (i.e., Warm Conveyor Belts, Mesoscale Convective Systems) that frequently develop equator-
ward of the jet stream are associated with vigorous vertical heating gradients that drive divergent outflow at the tropopause
(Wernli and Davies, 1997; Baumgart and Riemer, 2019; Steinfeld and Pfahl, 2019). The irrotational wind field established by
large-scale cloud systems is preferentially directed towards the jet stream, causing it to perturb polewards and enhance wind
35 speeds (Grams and Archambault, 2016; Steinfeld and Pfahl, 2019). This is a key mechanism by which forecast errors along
the jet stream manifest (Baumgart and Riemer, 2019; Berman and Torn, 2019). Using a potential vorticity (PV) perspective,
the warm and moist air that is brought to the tropopause in these cloud systems can be visualized as an enclosed area of low,
but positive PV (in the Northern Hemisphere). The advection of this low PV air towards the jet stream, a region of higher PV,
serves to sharpen the mid-latitude PV gradient. This sharpening of the PV gradient is the mechanism by which wind speeds
40 can be strengthened and lead to the enhanced westerly propagation of Rossby waves (Harvey et al., 2016).

The PV perspective has also been applied to study mesoscale and convective scale weather systems (Hertenstein and Schu-
bert, 1991; Braun and Houze Jr, 1996; Conzemius and Montgomery, 2009; Chagnon and Gray, 2009). Case-study investi-
gations have shown the presence of mesoscale areas of negative PV (NPV) along the tropopause in the mid-latitudes of the
45 Northern Hemisphere (Rowe and Hitchman, 2016; Oertel et al., 2020; Harvey et al., 2020). However, large-scale vertical heat-
ing gradients cannot lead to the generation of NPV as determined by the theory of PV impermeability (Haynes and McIntyre,
1990). Instead, it is proposed that NPV arises where the length scale of diabatic heating is spatially smaller than the flow that
the heating is embedded within. An example of this environment involves convective storms embedded within large-scale flow
(Weijenborg et al., 2015). Harvey et al. (2020) show a mathematical proof that expands on PV impermeability theory, denot-
50 ing that at large Rossby number scales, convective-scale PV dipoles (one of which is negative) form as a result of horizontal
heating gradients. At these scales, horizontal heating becomes of parity or of greater relevance than vertical heating gradients.
When horizontal heating is embedded within pronounced vertical wind shear, the PV dipoles can be tilted onto the vertical
plane (Chagnon and Gray, 2009). Composite studies verify that PV dipoles (and subsequently NPV) are a robust response
to convective updrafts within thunderstorms (Weijenborg et al., 2017) and warm-conveyor belts with embedded convection
55 (Oertel et al., 2020). Additionally, Harvey et al. (2020) propose that PV dipoles may also arise within narrow, strips of strong
diabatic heating, such as within the convective-rain bands of warm-conveyor belts.

It is inferred that observations of mesoscale bands of NPV along the tropopause may initially have their origin at comparatively smaller length scales. Oertel et al. (2021) demonstrate that a strong upper-level jet and vertical wind shear are key
60 ingredients to elongate convectively generated NPV onto larger scales. Namely, horizontal shear acts to deform and expand the convectively generated NPV, diluting NPV along the tropopause towards less negative values of PV, but does not change its sign (Oertel et al., 2020). Instead, mesoscale NPV can persist for several hours as it is advected along the jet steam at a near-zero, but negative PV unit (PVU) value. These bands of persistent NPV are characterized by regions of anticyclonic relative vorticity that are of higher magnitude than planetary vorticity, drawing comparison to inertial instability theory (Rowe and
65 Hitchman, 2016; Oertel et al., 2020). Once NPV elongates towards the mesoscales, it has been observed to locally strengthen wind speeds and perturb the jet poleward (Rowe and Hitchman, 2016; Blanchard et al., 2021). Elongated NPV has also been linked to instances of clear-air-turbulence (Trier and Sharman, 2016; Lee et al., 2023) and the introduction of synoptic-scale numerical model errors associated with non-divergent winds along the jet stream (Lojko et al., 2022).

70 While the interaction of elongated bands of NPV with the jet stream appear dynamically relevant and may have important practical applications for aviation and numerical weather prediction, the majority of the aforementioned studies largely utilize case-study perspectives to demonstrate how NPV interacts with the jet stream. A composite analysis is proposed herein to provide a climatological perspective on NPV and to complement previous case-study investigations by verifying whether the amplification of the jet stream is in fact a robust response to NPV interactions. Two key questions are proposed via the
75 composite analysis:

- What are the climatological characteristics of elongated bands of NPV when they interact with the jet stream?

- Which dynamical mechanisms involved in jet stream amplification are present when NPV interacts with the jet stream?

The analysis will focus on the Western North Atlantic jet stream region. This region has been shown to be frequently associated with convective storms (Li et al., 2020) and warm conveyor belts (Madonna et al., 2014), which are candidate weather
80 events for the generation of NPV (Clarke et al., 2019; Oertel et al., 2020). Another rationale for focusing on this specific region is that previous composite studies have identified the Western North Atlantic as a mid-latitude climatological hotspot for inertial instability (Thompson et al., 2018) along the tropopause.

The paper is structured such that the data and methodology is presented in Section 2. The climatological characteristics of
85 NPV are presented in Section 3.1. The large-scale circulation patterns during NPV-jet interactions are evaluated in Section 3.2. Three detailed case-studies of synoptic-scale NPV that focus on the dynamics involved in NPV-jet interactions are presented in Section 3.3. A discussion of synoptic-scale NPV is had in Section 4 with particular focus on its relevance for the large-scale atmospheric circulation. The work is concluded in Section 5.

2 Data & Methods

2.1 Data

The ECMWF reanalysis version 5 (ERA5; Hersbach et al., 2020) is downloaded at a grid spacing of 0.25° (∼31 km) for the years of 2000 – 2021. The fine grid spacing and temporal resolution of ERA5 compared to other global reanalysis datasets provides an opportunity to study mesoscale NPV features in a climatological framework. PV, geopotential height (Z), horizontal winds and integrated vapor transport (IVT) with 6-hourly resolution are available directly from the ERA5 archive. Data is predominantly obtained at 250 hPa to focus on how NPV interacts with the mid-latitude tropopause. While it is more common for PV analysis to be performed on isentropic levels, the isentropic level associated with the tropopause can vary notably with respect to season (Röthlisberger et al., 2018). Using only one particular isentropic level can miss NPV features depending on the season examined. Hence, for simplicity, a single isobaric level that is representative of the tropopause at all seasons is selected as isobaric surfaces near the tropopause tend to vary less with height. It is also noted that elongated bands of NPV are maximized in frequency along shallow layers of the tropopause (fig. A1). Prior to any further climatological analysis, the latitude and longitude data are filtered across the Western North Atlantic (25°N, 100°W)–(65°N, 50°W). An additional 10° buffer is kept on each side of the domain to minimize any boundary effects when identifying NPV features.

2.2 Methods

2.2.1 PV-Jet Interaction Algorithm

An algorithm is designed to search for elongated NPV features that reside in close proximity to the jet stream. Henceforth, these instances are termed NPV-jet interactions. The algorithm is split into three parts. First, the identification of elongated NPV features. Second, the identification of jet stream features and last, identification of interactions between elongated NPV and the jet stream. A schematic is provided below (Fig. 1) to give a general overview of the methodology. PV data is bilinearly interpolated to 0.5° to improve computational efficiency. This interpolation has no impact on the final results relating to the frequency of NPV-jet interactions.

The first step in the algorithm is to identify and label all connected regions of NPV, specifically where PV is =< -0.01 PVU. The major axis length-scale is calculated for each label. Only the longest 2% of features are kept. This threshold corresponds to NPV length-scales longer than 1650 km (Fig. 2a). These features are henceforth referred to as a synoptic-scale NPV features. As a sanity check, the 97th and 99th percentile are also tested; however, these thresholds do not impact conclusions made regarding NPV-jet interaction frequency. The final step involves obtaining and saving the coordinates of the synoptic-scale NPV features.
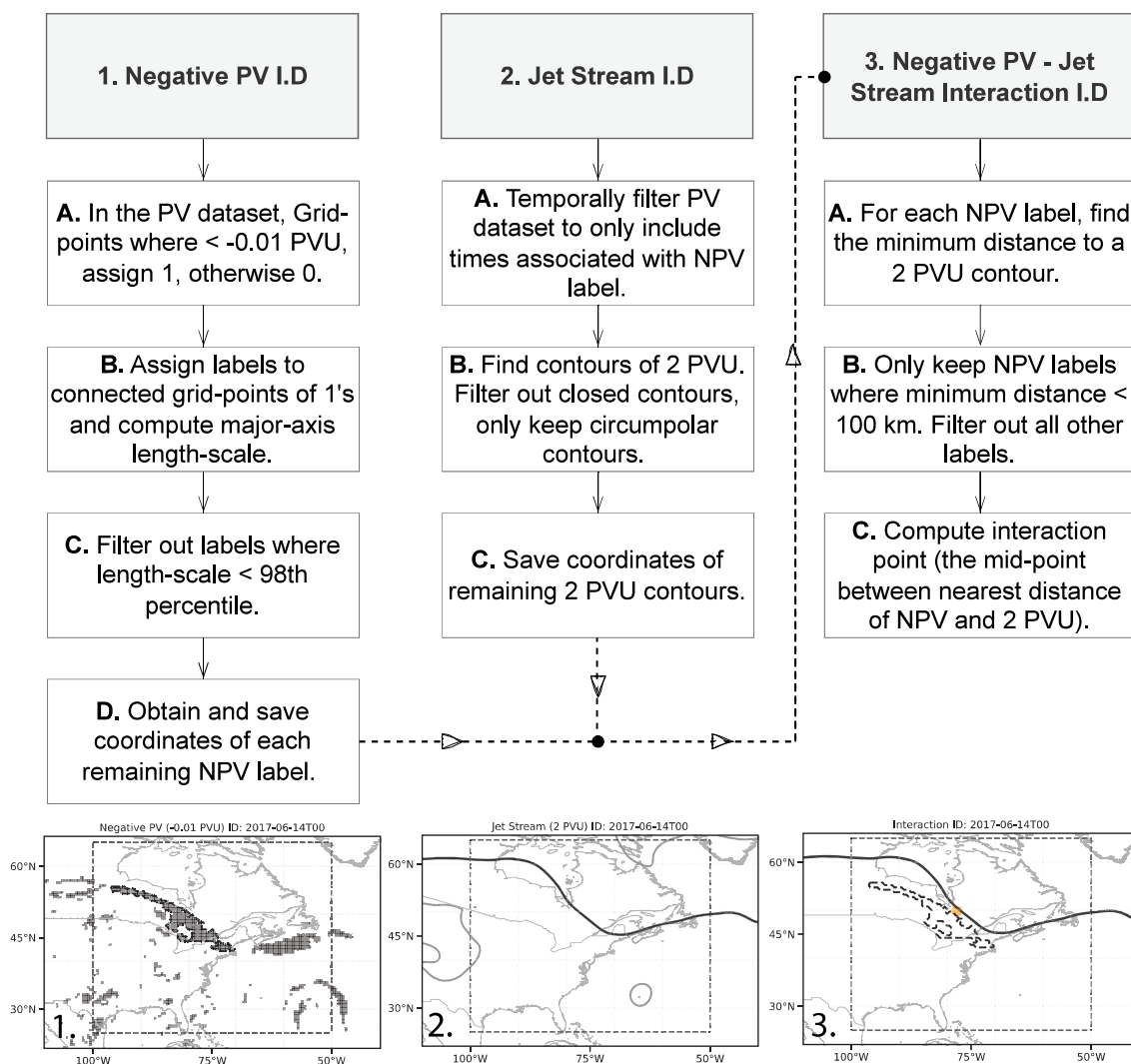
Figure 1. Schematic overview of the NPV – Jet Interaction Identification Procedure outlining three key steps in the algorithm design. The images at the bottom of the schematic denote how the algorithm works on a single case. Grey shading shows individual NPV labels. Dark dashed contours denote the perimeter of synoptic-scale NPV features. Dark, continuous contours illustrate the 2 PVU contour (jet stream). The orange circle denotes the 'interaction-point', which is defined as the mid-point coordinate between the closest coordinate associated with the NPV feature and the jet stream. The grey dashed box shows the domain over which NPV-jet interactions are searched for. NPV in the 10° boundary region of the box is also retained for the composite analysis to minimize boundary effects.

For jet stream identification, contours where the PV field has a value of 2 PVU are identified. This is a common choice for identifying the jet stream (Barnes et al., 2010). Prior to jet stream identification, time-steps in which no synoptic-scale NPV features were identified are filtered out. Next, the PV field is smoothed by a 10 point Gaussian smoother to improve contour identification by smoothing out mesoscale PV filaments. Further filtering of contours is applied by only keeping circumpolar

125   contours. Circumpolar contours are defined as continuous contours of 2 PVU that extend across the longitudinal extent of the NPV-jet interaction domain. Non-continuous contours are likely associated with cut-off features (Hoskins, 1997) and are chosen to be removed. A small subset of times (4 time-steps) were not able to identify continuous 2 PVU lines. These times were also filtered out from the analysis. The remaining 2 PVU contour coordinates are saved for evaluation with respect to the NPV coordinates.

130

A simple distance metric is used to define time-steps when synoptic-scale NPV interactions occur with the jet stream. For each time-step, we use the coordinates from the NPV feature and 2 PVU contour to find the point of minimum distance between the two features. The minimum distance coordinate is referred to as the point. If a coordinate of a NPV feature is within 100 km to the jet stream, it is kept. If the minimum distance between NPV and 2 PVU exceeds 100 km for a particular event,

135   the event is filtered out. Subsequently, locate the interaction point's coordinates (latitude, longitude). Stronger jet stream winds were present when using a threshold of 0-100 km distance compared to 100-200 km and 200-300 km, motivating the selection of the 100 km threshold as NPV may be more dynamically relevant for jet stream dynamics at these shorter distances. The threshold sensitivity tests are shown in fig. B1. Sometimes, multiple synoptic-scale NPV features are detected within the 100 km threshold for a particular time-step. In these instances, all NPV features are retained for climatological analysis as long as

140   they are within the 100 km threshold. However, when computing centered composites, the NPV feature that is closest proximity to the 2 PVU contour is selected for identification of the minimum distance coordinate. It is additionally worth mentioning that in instances of consecutive time-steps with NPV-jet interactions, no temporal filtering is applied.

In total, 21341 synoptic-scale NPV features are detected within the domain during the 22 year time-period. From those, 4983

145   (23%) synoptic-scale NPV features are detected within 100 km of the 2 PVU contour. Some statistics of the NPV features are detailed in fig. 2.Figure 2a shows a histogram of the major-axis length of all NPV features detected. Over 80% (more than 10^6) of identified NPV features in ERA5 are characterized by a major-axis length shorter than 200km. The synoptic-scale NPV features retained in study are of much larger length-scales than the mesoscale filaments described previously in literature (Oertel et al., 2020; Blanchard et al., 2021). ERA5 will smooth the NPV field, enabling it to more consistently detect synoptic-scale

150   NPV features with respect to the aforementioned literature which use model output from convection resolving simulations, causing the PV field to be noisier.

For additional reference, the area sizes of all NPV features is plotted in fig. 2b. The area size of NPV features largely follow the distribution of major axis length scale (fig. 2a). The majority (over 90%) of NPV features are smaller than 1 x 10^5 km^2 in

155   area size. Figure 2c shows all the distance between synoptic-scale NPV with respect to the jet stream for each synoptic-scale
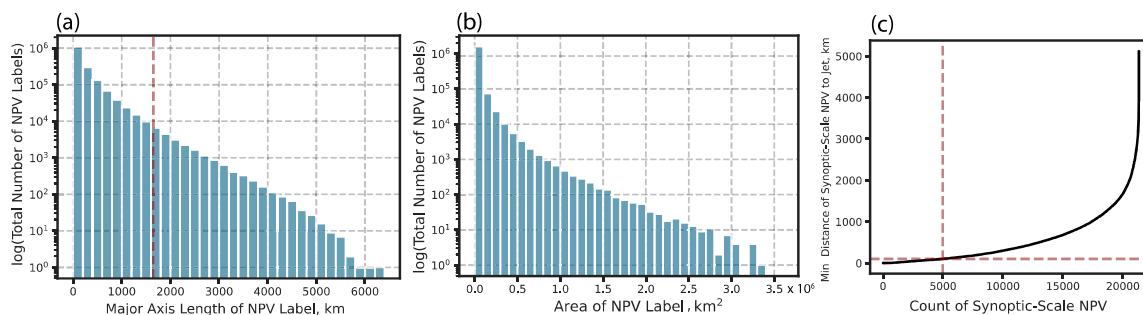
Figure 2. Statistics of the identified NPV objects. (a) The total number of NPV objects detected in ERA5 on the y-axis (logged) and the major axis length scale (km) of each NPV object binned into intervals of 200 km. The red dashed lines show where the 98th percentile lies for the major-axis length scale. (b) is the same as (a) but with the area size ($\times 10^6$ km^2) shown on the x-axis. Binning intervals are set to 0.1×10^6 km^2. (c) shows the distance between each synoptic-scale NPV feature identified and its closest proximity to the jet stream. The red dashed line is used to show where the 100 km threshold lies for NPV-jet interactions (horizontal) and how many NPV-jet interactions are identified within the 100 km threshold (vertical).

NPV feature identified. The frequency of synoptic-scale NPV features decreases exponentially with distance away from the jet stream. (>25%) of synoptic-scale NPV features are detected within 100 km to the jet stream. Of the 32144 time-steps that comprise the period of study, 14580 have a synoptic-scale NPV feature within the domain (45% of the time). 3845 time-steps have a synoptic-scale NPV feature that is within 100 km to the jet stream (12% of the time-steps detect an NPV-jet interaction).

160

2.2.2 Composite Approach

The purpose of the centered composite approach is to identify the typical circulation patterns and kinematic phenomena when synoptic-scale NPV interacts with the jet stream. When computing the centered composite, the mean interaction point is computed from all events. Subsequently, all events are shifted towards the mean using a latitude weighting following Winters (2021).

165

A problem that arises when computing a mean composite is that important circulation pattern features become smoothed. When computing a principal component analysis on the PV field of all retained events, the dominant modes of variability are characterized by ridging environments (not shown). In contrast, computing a single mean composite illustrates zonal flow. This is due to the synoptic-scale NPV features arising in different locations within the ridging environment, hence the composite which is centered on the location of NPV-jet leads to too much smoothing on the ridge. To mitigate this effect, K-means clustering is applied to separate events into distinct circulation patterns. The K-means clustering is informed by the latitude weighted, PV field. The size of the domain used in the clustering algorithm was a 10°x10° box centered on the interaction coordinate.

170

Enlarging the domain (15°x15° and 20°x20°) had no discernible impact on the K-means clustering results.

175

The number of clusters selected is informed both objectively and subjectively. Modifying the methodology of Grazzini et al. (2020), the Silhouette score is used as an objective metric to determine the optimal number of clusters to use in this study. The Silhouette score metric evaluates how closely grouped together events are to each cluster centroid. The metric ranges from a score of -1 (poor clustering) to 1 (fully separated clusters). A value of 0 indicates that events tend to equally resemble other cluster centroids (i.e., equal distance to more than one cluster). The Silhouette score is computed for two-eight clusters. Two clusters provides the highest Silhouette score (0.24). However, it was noted that the interaction point was located in the same region (along the western flank of the ridge) for both of the clusters, so there was not a lot of variability in the location of NPV-jet interactions. Three, four and five clusters provided the next best Silhouette scores (0.18, 0.16 and 0.17 respectively). While the use of more clusters reduced the Silhouette score (the large-scale circulation patterns became more similar between each cluster) , there was more variance in the location of the NPV-jet interaction location. Increasing the number of clusters to three enhanced led to an interaction point being located along the eastern flank of the ridge in one of the clusters. Increasing the number of clusters to four and five did not improve the variability of the interaction point, hence three clusters was subjectively deemed appropriate for the analysis.

2.2.3 Kinematic Analysis of NPV

190

Several methods are used to interpret the impact of NPV on the large-scale flow. Amplification of the jet stream by different components of the wind is examined by calculating PV advection by the irrotational and non-divergent wind (Archambault et al., 2013) at 250 hPa. The partitioning of the winds into these two components is completed via Helmholtz partitioning using the Python Package, Windspharm (Dawson, 2016), which utilizes spherical harmonics on the global domain. The PV advection fields are computed for each event prior to applying the composite approach.

195

The wave activity flux (WAF; Takaya and Nakamura, 2001) is computed for each NPV-jet time-step to explain the relevance of how NPV enhances kinetic energy along the jet stream. The horizontal form of WAF can quantify the propagation and energy transport associated with horizontally propagating atmospheric waves along a single level of the atmosphere. WAF assumes quasi-geostrophy and is often used in the evaluation of large-scale flow patterns, particularly in the study of atmospheric Rossby waves and their downstream propagation. The WAF equation is shown below:

200

$$\overrightarrow{W} = \frac{1}{2|\overrightarrow{U}|} \begin{pmatrix} U[(\psi_x^{'2} - \psi' \psi_{xx}') + V[\psi_x' \psi_y' - \psi' \psi_{xy}'] \\ U[\psi_x' \psi_y' - \psi' \psi_{xy}'] + V[\psi_x^{'2} - \psi' \psi_{xx}'] \end{pmatrix} \tag{1}$$

U and V denote the base state wind in the zonal and meridional direction, where the base state is determined from the seasonal climatology: Boreal Winter, Spring, Summer and Autumn (DJF, MAM, JJA, SON). $|\overrightarrow{U}|$ is the wind speed. ψ' is the

streamfunction anomaly. $\psi^{'}$ is computed from ERA5 wind data using the Windspharm package. The x and y derivatives relate

205 to latitude and longitude. xx, xy and yy denote second deviate terms.

As mentioned above, 2D WAF is a quasi-geostrophic and dry kinematic metric. While the generation of NPV implies diabatic activity, once NPV grows onto mesoscales, it has been observed to persist quasi-adiabatically with a negligible change to PVU (Oertel et al., 2020; Lojko et al., 2022). Hence, a dry kinematic approach is assumed to be an appropriate framework to

210 use in the study of the synoptic-scale NPV. Individual components of the WAF equation can be assessed to understand the dry, dynamical mechanism by which NPV influences the magnitude of 2D WAF.

The first terms inside the square bracket refer to momentum transport. This is computed from the square of the non-divergent wind terms. Given that NPV has been associated with jet streaks, enhanced momentum transport when NPV is in close proxim-

215 ity to the jet stream is expected. The second terms refer to the ageostrophic flux of geopotential (Takaya and Nakamura, 2001), and denotes a source or sink for wave activity (Orlanski and Katzfey, 1991). $\psi^{'}_{xx}$ and $\psi^{'}_{yy}$ are of particular interest and represent shear anomalies approximating to the v_x and u_y terms of the relative vorticity equation. It is expected that these terms will be magnified in regions of NPV due to NPV's close relationship to anticyclonic vorticity minima (Lojko et al., 2022). A partitioning of the WAF equation will be performed to mechanistically illustrate the relationship between synoptic-scale NPV and WAF.

220

One additional technique that is used involves relative vorticity inversion (Oertel and Schemm, 2021) to illustrate the circulation pattern associated with a spatially confined relative vorticity field. NPV can not be inverted via PV inversion as it is dynamically unstable (Davis and Emanuel, 1991; Davis et al., 1993; Oertel and Schemm, 2021). In contrast, relative vorticity inversion is independent of the sign of the relative vorticity field. The relative vorticity is equal to the Laplacian of the

225 streamfunction on a horizontal surface. Solving the Poisson equation, and using the streamfunction's relation to vorticity, the non-divergent winds can be obtained along a horizontal, 2D surface (i.e., at 250 hPa) (Oertel and Schemm, 2021). This is particularly useful in examining synoptic-scale NPV, as it appears to largely be a shallow-layer feature that resides within the upper troposphere (Fig. A1).

230 ## 3 Results

3.1 Climatology of NPV over the West Atlantic

The climatological frequency of NPV frequency are presented for the North American-West Atlantic region in fig. 3. Figure 3a shows the frequency of all NPV identified using ERA5 regardless of size or distance to the jet stream. A meridional gradient of NPV frequency is observed with a maximum in the sub-tropics (>12%) that decreases towards higher latitudes, where the

235 frequency drops below 4% northward of 50°N. This gradient largely follows the general pattern of mesoscale convection observations Li et al. (2020). The higher frequency of NPV at lower latitudes is also consistent with maxima in inertial instability

frequency Thompson et al. (2018) where anticyclonic relative vorticity is of greater magnitude than the Coriolis parameter.

Other spatial patterns, such as effects of topography, are also captured in the NPV frequency distribution. A low percentage of NPV frequency west of the Rocky Mountains (100°W) sharply transitions into a region of higher NPV frequency farther east until reaching a maximum over the coastal Western Atlantic (NPV frequency >9%). This maximum is co-located with warm Gulf Stream waters that can drive vigorous diabatic weather systems (Minobe et al., 2008) and coincide with climatological hotspots of warm conveyor belts (Madonna et al., 2014)

The spatial distribution and percentage frequency of NPV changes when focusing on synoptic-scale NPV-jet interaction events (Fig. 3b). NPV-jet interactions are most frequent about the mid-latitudes, a maximum (>1.2%) is located over the coastal Western Atlantic about 41°N, 65° W. Generally, NPV-jet interactions are frequent about the Coastal Western Atlantic along a latitude band of 40°N. The location of maximum NPV-jet frequency coincides with the frequent occurrence of warm-conveyor belts (Madonna et al., 2014) and the occurrence of latent heating maxima attributed to mesoscale convection (Li et al., 2020).

To motivate the link of NPV-jet interaction events to amplification of the jet stream, fig. 3c shows the mean difference in wind speeds between NPV-jet interaction events and all other time-steps. A diagonal band of stronger winds stretches from the Gulf of Mexico (>2 m s^{-1}) up to Eastern Canada. Wind speeds are maximized at 5 m s^{-1} at approximately 50°N, 65°W, about 8°N of the maximum frequency of NPV-jet interactions (fig. 3b). The shaded pattern in wind speed difference is statistically significant at the 98th percentile upon computing a two sided student t-test with respect to climatology.

NPV-jet interaction frequencies exhibit a pronounced seasonal cycle. DJF is associated with the most frequent NPV-jet interactions (fig. 4a) with NPV-jet interaction frequencies exceeding 2.5% over the Western Atlantic. MAM NPV-jet frequency (fig. 4b) maxima reduce to 1.25% and shift westward towards the Eastern US coastline. JJA frequency maxima (fig. 4c) of 0.5% are predominantly located over continental North America. SON (fig. 4d) NPV-jet frequency maxima exceeding 1.5% is predominantly located over the Western Atlantic. The spatial location of the seasonal frequency patterns suggest that JJA NPV is predominantly dominated by continental convection. In contrast, the location of the wintertime NPV features over the West Atlantic is consistent with the aforementioned warm conveyor belt climatology. It is also noted that the spatial seasonal variations of NPV-jet maxima agree with the location of air masses that contribute to downstream blocking (Pfahl et al., 2015; Steinfeld and Pfahl, 2019), which are postulated to arise from rapidly ascending air-streams in regions of strong latent heating. The seasonal co-location of NPV with the Steinfeld and Pfahl (2019) climatology is not necessarily surprising as NPV is a byproduct of latent heating within convective weather systems (Harvey et al., 2020; Oertel et al., 2020).

Additional detail on the seasonal and spatial climatology of all NPV and NPV-jet interactions is provided in fig. 4e-f. For all NPV features in the domain (fig. 4e), the total monthly area coverage of NPV demonstrates a seasonal cycle. NPV area coverage is maximized in October and minimized in February. JJA has higher NPV area coverage in the domain compared to
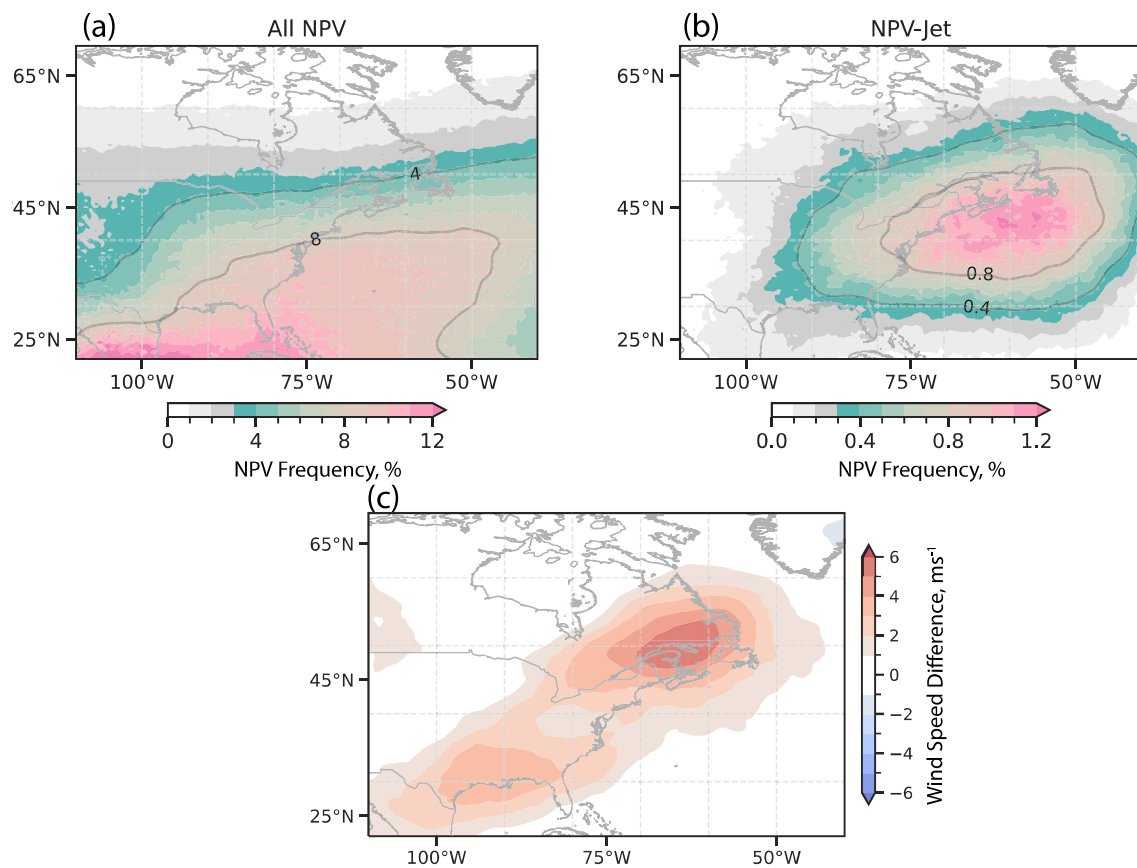
Figure 3. Climatological frequency of NPV between 2000-2021 is shown in (a) and (b). (a) shows the percentage of time NPV is observed at a grid-point irrespective of its size. (b) shows NPV-jet frequency (98th percentile size NPV features within 100 km of the jet stream). (C) shows the mean wind speed difference between NPV-jet interaction events and no NPV-jet interaction events.
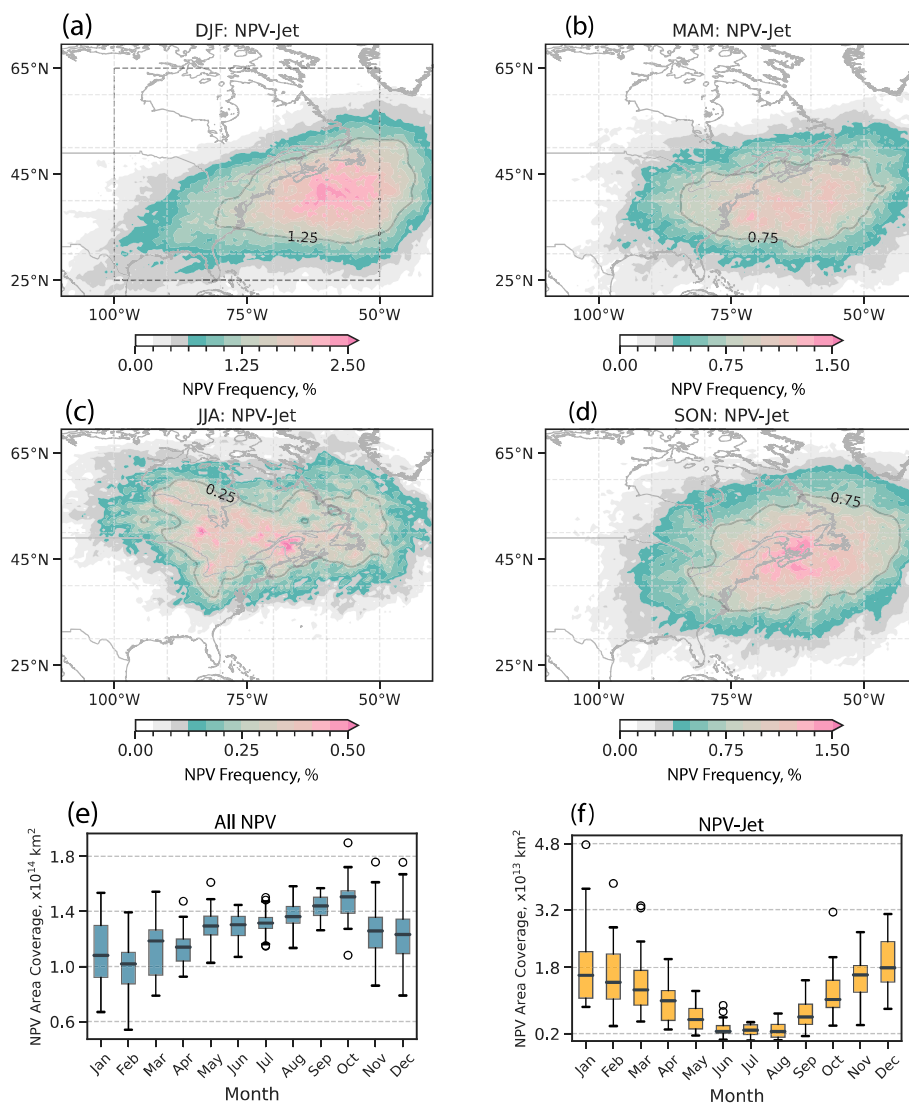
Figure 4. As in Fig. 3b but showing the seasonal frequency of NPV-jet interactions between 2000-2021 (a) for DJF, (b) MAM, (c) JJA, and (d) SON. (e) and (f) show boxplots of the monthly area covered by all NPV and NPV-jet interactions, respectively. Area coverage is computed within the dashed box domain (25°N, 100°W)–(65°N, 50°W). The whiskers of the box plot denote the upper and lower extrema. The top and bottom of the box denote the upper and lower quartile. The horizontal lines within the box illustrate the median area coverage.

DJF, although, interannual variability in NPV coverage during DJF is larger and can exceed JJA area coverage for particular years. It is also noted that the total area coverage for all NPV and NPV-jet interactions is sensitive to the location of the domain. When experimenting with shifting the domain westward, the summer (winter) month frequencies increase (decrease).
275 This relationship reverses when moving the domain eastward.

In fig. 4f, the seasonal cycle for area coverage for NPV-jet interactions is shown. In contrast to the area coverage of all NPV occurrences, the area coverage of NPV is now maximized during DJF alongside maxima in interannual variability. JJA has a minimum in area coverage and an order of magnitude lower area coverage and interannual variability in area coverage
280 compared to DJF. The rapid decrease in NPV-jet area coverage from MAM to JJA is consistent with the climatological, rapid decrease of jet stream wind speeds over the USA (Iqbal et al., 2018). The much lower frequency of JJA NPV-jet area coverage suggests synoptic-scale NPV is much less frequent during summer months. The absence of strong jet stream winds is suspected to limit the upscale growth of NPV (Oertel et al., 2021). A weaker jet stream provides a plausible explanation for the lower frequency of synoptic-scale NPV during JJA despite larger total area coverage when accounting for all NPV sizes
285 during JJA. Conversely, more frequent, isolated convection during the summer months may result in an increased frequency of sub-mesoscale NPV features. The wind speed difference plot (fig. 3c) was also recomputed for each season. It was noted that the wind speed differences shifted in accordance with the seasonal location of NPV-jet maxima (not shown).

Linear trend analysis for NPV frequency from 2000 to 2021 shows an increase in NPV frequency (Fig. 5a), whereby much
290 of the increase is attributed to a narrow latitude band between 35°N-45°N, coincident with the maximum in NPV-jet interaction frequency (fig. 3b). An increasing, relative trend of 1% per year extends from 100°W-50°W, and farther downstream into the Atlantic. Localized maxima of 3% per year in the trend can be observed over the Eastern USA and Coastal Western Atlantic, with an additional increasing trend area that encompasses the Gulf of Mexico and Southern USA (Over a 22-year time-period, this equates to a relative increase of 66% in some localized regions).
295

The relative trend in NPV-jet interactions is weaker but also positive (Fig. 5b), with maxima values exceeding 0.5% per year (a relative increase of 11% over a 22 year time period). Interestingly, these values coincide with maxima in the trend for all NPV events, predominantly over the Eastern USA and Coastal Western Atlantic. The increasing trend is also generally contained within a narrow latitude band between 35°N-45°N, suggesting that the overall trend is driven in part by synoptic-scale
300 NPV features that develop adjacent to or are advected and interact with the jet stream. Unlike fig. 5a, however, the observed increasing trend over the 22-year time period does not satisfy the false discovery rate.

Addressing the interannual area coverage of all NPV events in the domain (Fig. 5c), much of the increasing NPV frequency occurs after 2010. Prior to 2010, interanual variability of NPV area coverage was considerably less compared to post 2010. In
305 contrast, the interannual variability is much more pronounced for NPV-jet interactions (Fig. 5b). 2010, 2016 and 2019 denote years with maxima in NPV-jet area coverage within the domain. As just 22-years of data are used the trend could be predomi-
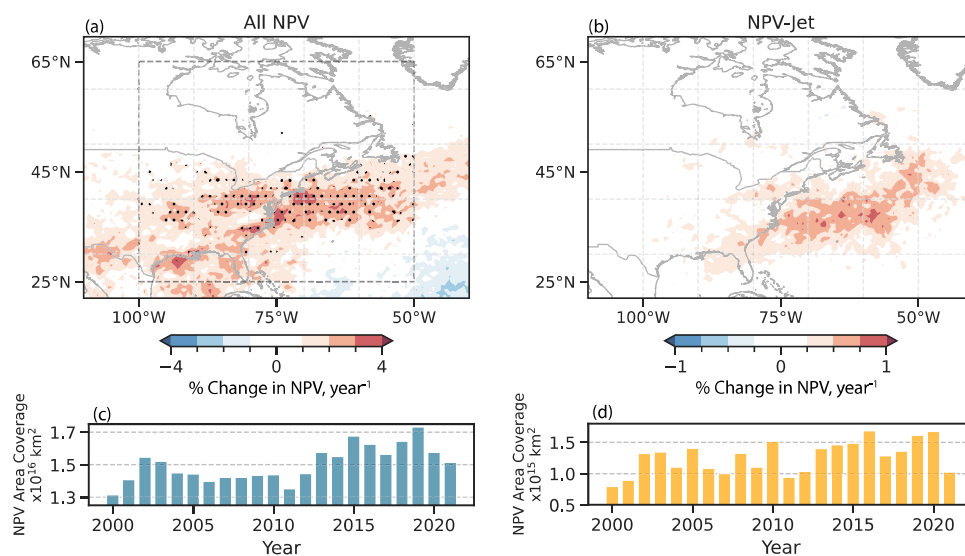
Figure 5. Interannual trend of NPV frequency from 2000-2021 expressed as a relative percentage change. (a) shows the total change in NPV frequency per year at each grid-point. (b) shows the same as (a) but for NPV-jet interactions. (c) and (d) shows the total area covered by all NPV (c) and NPV-jet interactions (d) per year within the domain (25°N, 100°W)–(65°N, 50°W). All shaded regions are statistically significant to the 98th percentile following the application of a student t-test. The false-discovery rate (Wilks, 2016) is also computed using the obtained p-values from the student t-test. The fraction of null hypotheses erroneously rejected is set to 0.1. Grid-points that satisfy the false discovery rate are stippled.

nantly influenced by decadal variability rather than longer term climatic trends. However, recent work published by Lee et al. (2023) denotes that NPV at 250 hPa during the winter months over the Western Atlantic has experienced a statistically significant (using a student t-test) increasing trend over a 40 year time-period starting from 1979. Additionally, Prosser et al. (2023) use a variety of metrics related to turbulence (including NPV) over the same 40-year time-period to illustrate a statistically significant increasing trend in turbulence over the Continental United States and Western Atlantic. Both of these studies are based on ERA5 data and support the results presented here that NPV-jet interactions have approximately increased by a relative amount of 11% from 2000-2021 about the climatological location of the jet stream.

3.2 Circulation Characteristics

To link NPV-jet interactions with distinct circulation pattern, a composite analysis leveraging the use of K-means clustering is performed. NPV-jet interaction events are separated into 3 clusters based on the pattern of the PV field within a 10°x10°

box centered on the interaction point. The three clusters reveal ridging environments with different amplitudes and phases (Fig. 6a-o). Cluster 1 shows an amplified ridge with a pronounced trough-ridge couplet. The interaction point is located on the westward flank of the ridge. Cluster 2 has a broader, ridge pattern with the interaction point also located along the westward flank of the ridge. Lastly, cluster 3 illustrates another pronounced trough-ridge couplet but with the interaction point located along the eastern flank of the ridge.

In fig. 6a-c, composites of the PV anomalies, PV gradient anomalies and the frequency of NPV-jet interactions are shown. The maximum frequency of NPV-jet events lie adjacent to the interaction point along the equatorward side of the jet (per definition of the composite). The interaction point is straddled by two PV anomalies of opposing sign. Note that to a first order, the anomalies predominantly result from the presence of the large-scale trough-ridge couplet. However, NPV features are embedded within the large-scale negative PV anomalies and should thus contribute to the NPV anomaly signal. Directly adjacent to the interaction point lies a region of positive PV gradient anomalies reaching maxima values in excess of 2.5 PVU per 100 km. The strengthened gradient lies on the polar side of the 2 PVU contour, where the PV gradient rapidly sharpens towards much higher PVU values.

In the second set of clusters (fig. 6d-f), composites of wind speed anomalies, upper-level geopotential anomalies (Z) and IVT anomalies are shown. In each cluster, the Z anomalies align with the location of the aforementioned PV anomalies. Cluster 1 has the most amplified trough-ridge couplet with both negative and positive Z anomalies reaching magnitudes of 150 m. Cluster 1 also coincides with the strongest IVT anomalies reaching values well in excess of 300 kg m^{-1} s^{-1}. The close proximity of the IVT anomaly adjacent to the trough indicates a favorable environment for large-scale ascent conducive to squall line and warm conveyor belt development (Dacre et al., 2019).

Cluster 3 involves NPV-jet interaction events in a comparatively drier region of the ridge (fig. 6f). Hence, moist processes are likely to be far less important for NPV-jet interactions within this cluster. The IVT anomaly in this case is weakest but still remains positive and in excess of 100 kg m^{-1} s^{-1}. The weakened IVT anomaly in this case partly results from the IVT being further away from the interaction point, thus becoming more radially smoothed out. Although, this cluster could also be indicating that the IVT anomaly tends to be weaker when synoptic-scale NPV interactions with the eastern flank of the ridge. Conceptually, the three clusters resemble the evolution of the synoptic-scale NPV feature from its initial formation along the westward flank of the ridge where strong diabatic processes (i.e., latent heating) dominate until its subsequent advection and downstream along the apex and eastern flank of the ridge (Oertel et al., 2020).

The composite of wind speed anomalies shows that all NPV-jet interactions are associated with wind speeds exceeding 50 m s^{-1} coinciding with the NPV feature (fig. 6d-f), no matter if synoptic-scale NPV is located on the poleward (fig. 6d-e) or equatorward (fig. 6f) flank of the ridge. The minimal IVT signal in fig. 6f suggests that the PV gradient sharpening and spatially coincident positive wind speed anomalies do not necessitate vigorous, in-situ moist-processes. Fig. 6d-e involve NPV-jet
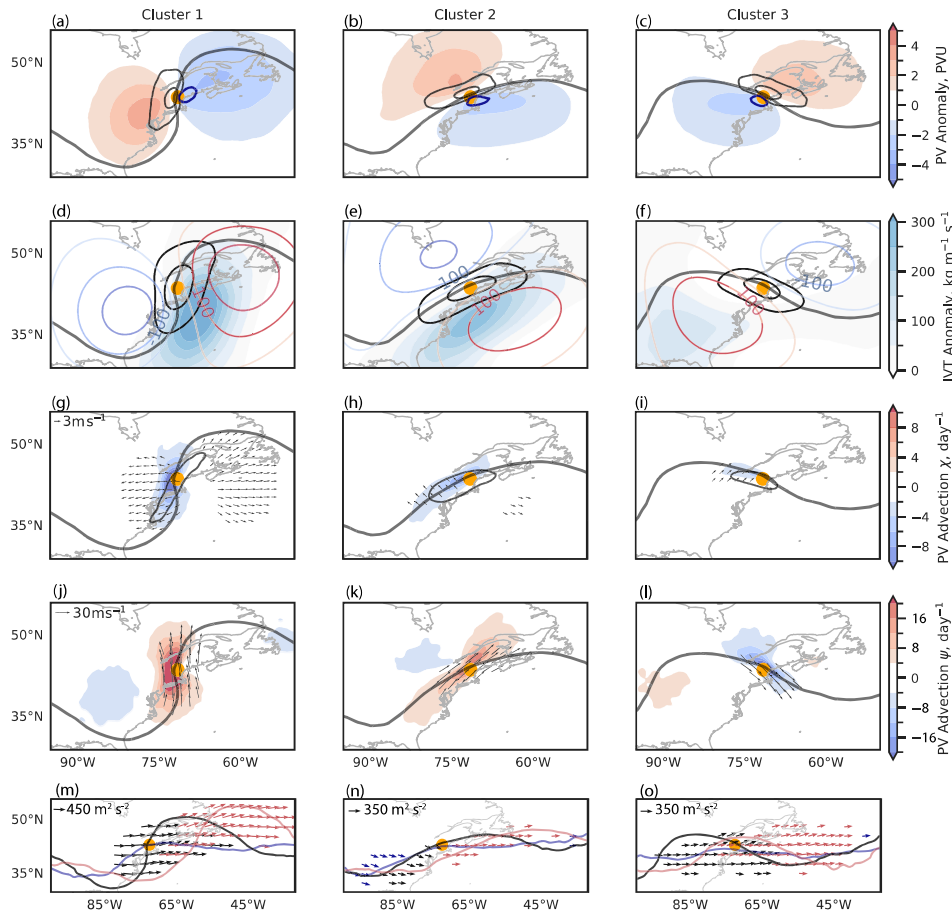
Figure 6. The k-means clusters (k = 3) derived from the weighted PV field at 250 hPa. Cluster 1 = 1136 cases, 2 = 1458 cases, 3 = 1251 cases. Fields are plotted at 250 hPa. The x and y axis represent a pseudo latitude and longitude as a result of performing a centered composite. (a-c) shows the PV anomaly computed from seasonal climatology (shaded, PVU) and the PV gradient anomaly (contoured in black with values of 1.5 and 2.5 PVU per 100 km displayed). Regions where NPV-jet frequency exceeds 60% is contoured in blue. (d-f) shows the IVT anomaly (shaded, kg m^{-1} s^{-1}), Z anomaly contours (red: +50, 100, 150 and blue: -50, 100, 150, m) and positive wind speed anomalies (black contour: 40, 50, m s^{-1}). (g-i) illustrates PV advection by the irrotational wind (shading, PVU per day), vectors plotted where irrotational wind anomalies >3 m s^{-1}. j-l shows the PV advection by the non-divergent wind (shading, PVU per day). Vectors plotted where non-divergent wind anomalies >30 m s^{-1}. m-o shows the lagged WAF. Black vectors show WAF on the day of interaction (>450 m^2 s^{-2} in m, >350 m^2 s^{-2} in n-o). Blue (red) arrows show WAF 24 hours before (after) interaction. The lagged 2 PVU contours are shown as a solid line with their respective colors.

interactions that overlap with a strong, positive IVT anomaly but of equatable wind speed anomaly magnitude as fig. 6f.

355   Figure 6g-i display the ageostrophic wind speed anomalies and PV advection by the irrotational wind (not anomaly). In each cluster, the positive ageostrophic wind anomaly exceeds 15 m s^{-1} and is centered on the interaction point, denoting that NPV-jet interactions are associated with highly ageostrophic environments. The ageostrophic wind speed magnitudes are of equatable magnitude for each cluster. It is interesting to note the elongated strip of positive ageostrophic wind speed anomalies that diagonally extend along the westward flank of the ridge in fig. 6g, although an explanation is not provided for whether this
360   is a realistic feature or an artefact of the centered composite.

    PV advection in clusters 1 denotes a strong contribution from the irrotational wind field to sharpening the PV gradient along the 2 PVU contour (fig. 6g). NPV interactions along the westward side of a ridge co-occur with regions of positive irrotational wind field anomalies (strong upper-level outflow) (fig. 6g-i). Coupled with positive IVT anomalies, the divergent outflow is
365   likely influenced by strong latent heating in this region. Cluster 3 (fig. 6i) differs with a weaker PV advection signal by the irrotational wind. The irrotational wind vectors do not directly lie over the 2 PVU line, suggesting a weak influence from the irrotational winds on perturbing the jet stream. Hence, NPV-jet interactions along the downstream flank of the ridge appear to be predominantly associated with PV advection by the non-divergent wind (Fig. 6j-l). To a first-order, the advection signal from the non-divergent wind is associated with the eastward advection of PV by the mean flow. The strongest signal in PV
370   advection by the non-divergent wind arises in Cluster 1, coinciding with stronger contribution from the irrotational wind field component (fig. 6g).

    Despite NPV being far away from the positive IVT anomaly in Cluster 3 (fig. 6f), positive wind speed anomaly maximum in the jet stream that are virtually the same in value as in cluster 1 and 2 (fig. 6d-e), providing evidence that the NPV is associated
375   with enhanced jet wind speeds without the insitu influence from moist processes associated with the positive IVT anomaly. Of course, there are other mechanisms co-occurring with the NPV feature, such as supergeostrophic winds around the apex of the ridge (Martin, 2014), which are not explicitly assessed through the composite analysis here.

    Lastly, the lagged WAF for each of the three clusters is shown in fig. 6m-o. 24 hours before NPV-jet interaction, the large-
380   scale circulation pattern consists of either a weakly amplified ridge (fig. 6m-n) or zonal flow (fig. 6o). WAF is relatively small, and does not exceed the WAF plotting threshold in fig. 6m and fig. 6o. During NPV-jet interaction, the ridge becomes more pronounced and amplified in all clusters. WAF vectors also emerge about the interaction point. The WAF packet emerges predominantly on the equatorward side of the jet stream in fig. 6n-o. Additionally, the WAF packet is displaced slightly upstream of the interaction point, closer to the base of the trough in fig. 6n Examining the WAF 24 hours later, the WAF packet per-
385   sists following its emission on the day of the NPV-jet interaction event. Furthermore, the WAF packet coherently propagates downstream in all 3 of the clusters, maintaining similar magnitudes as on the day of the NPV-jet interaction. This maintenance of the amplified WAF packet coincides with the maintenance of the more amplified ridge that is of comparable magnitude to

the day of NPV-jet interaction. To show the link between synoptic-scale NPV with the emergence of enhanced WAF, the WAF
equation is partitioned in the following section to mechanistically illustrate how NPV amplifies the jet stream.

3.3 Archetype Case-Study Analysis

The composite approach is not well suited for evaluating the evolution of temporally fast, mesoscale features. A case-study
approach is favored to further illustrate the kinematic impacts of NPV on the jet stream for each cluster. Three archetype
cases are selected that are most representative of their corresponding cluster. Archetype cases are identified using a Euclidean
distance metric (lower Euclidean distance denotes greater similarity to the cluster's mean PV field). From 10 cases for each
cluster that best resemble the mean PV field, one case for each cluster is subjectively selected. The subjectively chosen cases
are deemed to be the best at highlighting the influence of NPV features on the jet stream. To summarize, three cases that best
represent their respective clusters are chosen to evaluate NPV-jet interactions through a detailed, wave activity flux perspective.

3.3.1 Synoptic Overview

In fig. 7a-c, a synoptic overview is provided for each archetype case. The large-scale circulation for each case illustrates a ridge
with strong IVT along its westward flank. fig. 7a-b depict a synoptic-scale NPV feature predominantly along the western flank
of the ridge, while the synoptic-scale NPV feature in fig. 7c is mainly located along the apex and eastern flank of the ridge.
For the second and third cluster, the NPV feature does not overlap with the region of strong IVT, implying the NPV feature is
away from the influence of in-situ, synoptic-scale latent heating. For each case, the point where NPV is in closest proximity to
the jet stream coincides with wind speed maxima. Wind speeds in excess of 70 m s^{-1} are observed in fig. 7b-c, and surpassing
90 m s^{-1} in fig. 7a).

Figure 7d-f analyzes relative vorticity and its inversion to assess the impact of NPV on the large-scale flow. Regions of an-
ticyclonic vorticity with a magnitude exceeding 1x10^{-4} s^{-1} are predominantly situated within the NPV features. On the polar
side of the 2 PVU line, strips of cyclonic vorticity are observed adjacent to the NPV feature for each case. An inversion of the
relative vorticity within the boxed domain predominantly results in an anticyclonic non-divergent wind field with wind speeds
maximized about the 2 PVU contour reaching values of 45 m s^{-1} in fig. 7d and fig. 7f. Figure 7e involves an NPV feature
adjacent to a strip of cyclonic vorticity exceeding 2 x 10^{-4} s^{-1} and a non-divergent wind maximum of 55 m s^{-1}. The vorticity
inversion elegantly illustrates the influence of the strong cyclonic vorticity in this case (fig. 7e). Namely, two dipoles rotating
in opposing directions are illustrated, resulting from the interaction between anticyclonic vorticity (associated with NPV) and
cyclonic vorticity on the polar side of the 2 PVU contour (Cunningham and Keyser, 2004; Pyle et al., 2004).

The wind speed magnitude derived from the inversion can account for over 50% of the maximum wind speeds in fig. 7a,
75% in fig. 7b, and 65% in fig. 7c. The vorticity inversion implies that the interaction between NPV and strips of cyclonic
vorticity on the polar side of the jet stream may dominate the total wind field signal. As a final test, the vorticity inversion was
exclusively performed over the region of NPV (without incorporating the influence of the cyclonic vorticity). Maximum non-
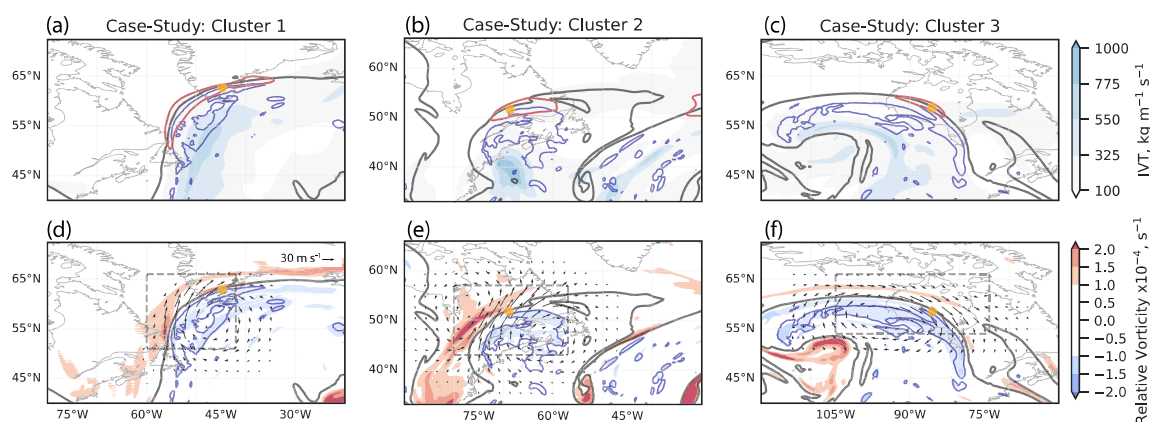
Figure 7. Meteorological Analysis of 3 cluster archetypes. The Cluster 1 Case (left column) occurs on: 2004-03-24 18 UTC, Cluster 2 Case (middle column): 2014-12-09 00 UTC, Cluster 3 Case (right column): 2021-05-24 00 UTC. In each figure, the 2 PVU contour (black line) and NPV (blue line) are shown. The orange dot illustrates the interaction point for each case (the coordinate at which the NPV feature is in closest proximity to the 2 PVU contour). a-c shows the IVT, kg m^{-1} s^{-1} (shaded), and wind speed contours in red at 70 m s^{-1} (the wind speed is contoured at 80 m s^{-1} in a). d-f shows relative vorticity (shaded), s^{-1}, and its subsequent inversion. The vectors show the non-divergent winds obtained from the vorticity inversion (computed within the grey, dashed box)

divergent wind speed values of 20 m s^{-1} were obtained for fig. 7d and 25 m s^{-1} for fig. 7e-f. In other words, the anticyclonic vorticity associated with NPV appeared to contribute about 50% of the total non-divergent wind field in the three cases. The maxima in the magnitude of the non-divergent winds attributed to NPV are larger compared to the 5 - 10 m s^{-1} attributed to a mesoscale NPV feature studied in Oertel et al. (2020). Although a different methodology was used in their study to quantify the influence of NPV on jet stream wind speeds based on 2-hourly wind circulation anomalies.

3.3.2 Individual Wave Activity Flux Terms

In this section, the terms that contribute to the total WAF equation are evaluated with respect to the synoptic-scale NPV feature. As the WAF equation is constructed from multiple different components (Eq. 1), the analysis is narrowed to focus on the first part of the WAF equation, $U(\psi_x^{'2} - \psi' \psi_{xx}')$ (although other terms will also be discussed when appropriate). As will be shown, these terms contribute the most to the WAF equation for each case.

In fig. 8a-c, the non-divergent wind field anomaly maxima is observed to lie adjacent to the NPV feature along the 2 PVU contour. Drawing insights from the vorticity inversion discussed in the preceding sub-section, it is suspected that the maxima in non-divergent wind anomalies stem from the dynamic interplay between the NPV feature and strong cyclonic vorticity on

the polar side of the jet stream. First, focusing on $\psi_x^{'2}$, which is found in $U(\psi_x^{'2}-\psi^{'}\psi_{xx}^{'})$, and the $\psi_y^{'2}$ momentum term, it follows that the maximum in momentum transport overlaps with regions of strong non-divergent wind anomalies. For each case, $\psi_y^{'2}$ (zonal momentum transport) is maximized along the zonal extent of the jet stream. The $\psi_x^{'2}$ term (meridional momentum transport) is most prominent along the meridional extent of the jet stream. For each case, these terms are maximized adjacent

440 to the NPV features. In the three cases presented, $\psi_x^{'2}$ exceeds 2000 m^2 s^{-2}, reaching its maxima precisely where the NPV feature is closest to the jet stream. The $\psi_x^{'2}$ term reaches 4000 m^2 s^{-2} where NPV is in closest proximity to the jet stream in fig. 8a . The larger magnitude of the $\psi_x^{'2}$ term in this case corresponds to the much stronger non-divergent wind anomalies observed along the entirety of the jet stream. It can be inferred that while the large-scale environment varies in its magnitude of momentum transport for different cases, the presence of NPV features appears to consistently coincide with a maximum in

445 momentum transport.

In fig. 8d-f, the ageostrophic geopotential flux is evaluated. Focus is placed on the $\psi^{'}$ and $\psi_{xx}^{'}$ terms of $U(\psi_x^{'2}-\psi^{'}\psi_{xx}^{'})$. The ridge is characterized by positive $\psi^{'}$ (I.e., a positive streamfunction anomaly). The $\psi_{xx}^{'}$ term is related to relative vorticity as it equates to a v$_x$ anomaly. In each case, this term largely overlaps with the NPV feature observed in fig. 8a-c. This is

450 because NPV is associated with a maximum in anticyclonic vorticity (fig. 7d-f). It can also be seen in fig. 8d-f that negative $\psi_{xx}^{'}$ overlaps with positive $\psi^{'}$. These two terms must be multiplied together to obtain $\psi^{'}\psi_{xx}^{'}$. In fig. 8e-f, $\psi^{'}\psi_{xx}^{'}$ is maximized within the ridge where overlap between $\psi_{xx}^{'}$ and $\psi^{'}$ occurs. In fig. 8d, $\psi_{xx}^{'}$ does not completely overlap with ψ', thus reducing contribution to $\psi^{'}\psi_{xx}^{'}$. In other words, NPV must be optimally embedded within a ridge environment such that anticyclonic shear can enhance the ageostrophic flux of geopotential.

455

In fig. 8g-i, $\psi_x^{'2}$ and $\psi^{'}\psi_{xx}^{'}$ are combined to obtain $U(\psi_x^{'2}-\psi^{'}\psi_{xx}^{'})$. Given that $\psi^{'}\psi_{xx}^{'}$ is negative when anticyclonic shear overlaps with a positive streamfunction anomaly, subtraction of this term following the sign convention in $U(\psi_x^{'2}-\psi^{'}\psi_{xx}^{'})$ means that $\psi^{'}\psi_{xx}^{'}$ becomes positive. In other words, the ageostrophic flux associated with anticyclonic shear is additive with the momentum term, $\psi_x^{'2}$. This means that $U(\psi_x^{'2}-\psi^{'}\psi_{xx}^{'})$ positively contributes to the WAF equation (assuming the base state wind, U, is positive). For each case shown in fig. 8g-i, the region where NPV interacts with the jet stream illustrates a maximum

460 in $U(\psi_x^{'2}-\psi^{'}\psi_{xx}^{'})$. It is proposed that this maximum arises due to the NPV feature dually enhancing momentum transport and the ageostrophic geopotential flux. In fig. 8g, the contribution to the $U(\psi_x^{'2}-\psi^{'}\psi_{xx}^{'})$ component predominantly arises from momentum transport, with ageostrophic geopotential flux becoming more dominant further away from the 2 PVU contour where momentum transport is minimized. In fig. 8h and fig. 8i, the ageostrophic flux term contributes more to $U(\psi_x^{'2}-\psi^{'}\psi_{xx}^{'})$

465 as a result of weaker momentum transport in the latter two cases.

3.3.3 Full Wave Activity Flux

Following the evaluation of individual terms in $U(\psi_x^{'2}-\psi^{'}\psi_{xx}^{'})$, the full WAF equation is now evaluated with respect to NPV-jet interactions. Figure 9a-c illustrate excellent agreement between the magnitude and spatial extent of the full WAF with respect
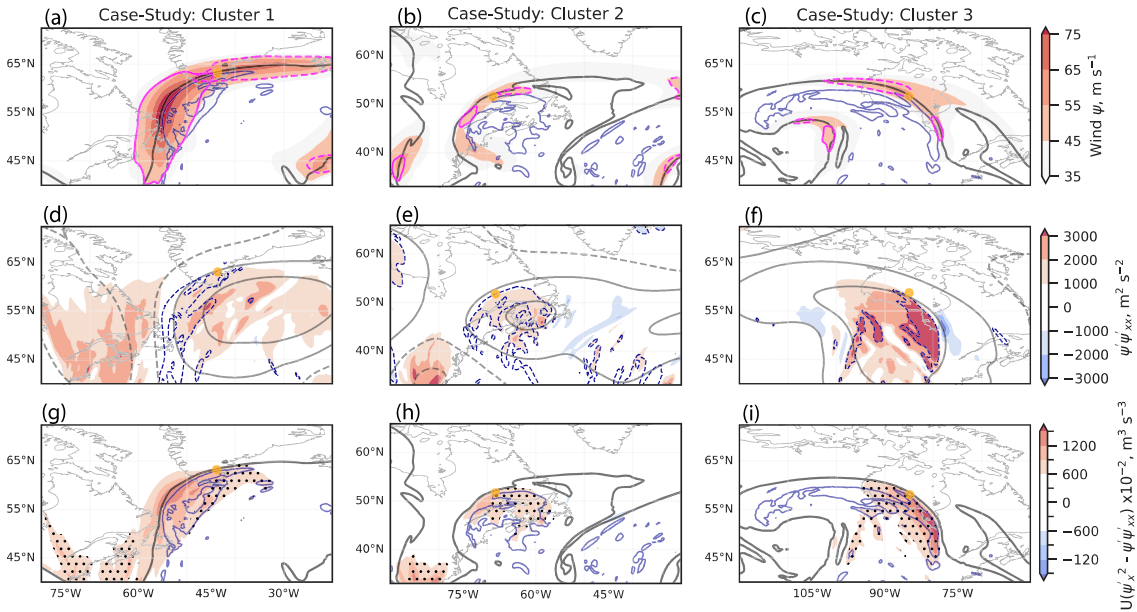
Figure 8. Component analysis focusing on the first term of the wave activity flux equation, $U(\psi_x^{'2} - \psi' \psi_{xx}')$. a-c focuses on momentum: The non-divergent wind anomaly, m s^{-1} is shaded in red, the magenta contours show the momentum transport anomaly terms at a threshold of 2000 m^2 s^{-2}. Solid contours denote meridional momentum, $\psi_x^{'2}$ while dashed contours show zonal momentum, $\psi_y^{'2}$. d-f examines the ageostrophic flux of geopotential. The solid (dashed) grey contours denote positive (negative) streamfunction anomaly, ψ' at intervals of +/- 1, 3x10^7 m^2 s^{-1}. The blue dashed contour denotes a negative shear anomaly ψ_{xx}' at -0.75x10^{-4} s^{-1}. The red shading illustrates the $-\psi' \psi_{xx}'$ term, relating to the ageostrophic flux of geopotential. The term is computed by multiplying the streamfunction anomaly and shear anomaly. Note that following sign convention in the WAF equation, a negative sign is placed at the front of $-\psi' \psi_{xx}'$. In g-i, the entirety of the $U(\psi_x^{'2} - \psi' \psi_{xx}')$ is shown in shading. Regions where $\psi' \psi_{xx}'$ is of larger magnitude than $\psi_x^{'2}$ are stippled.

470   to the $U(\psi_x^{'2} - \psi' \psi_{xx}')$ component (fig. 8g-i). WAF is maximized about the 2 PVU contour in fig. 9a where momentum transport dominates the contribution to the WAF equation in the case-study for Cluster 1 (fig, 8g). In contrast, WAF is maximized inside the NPV feature in fig. 9c, where the ageostrophic flux plays a more dominant role over momentum transport (fig. 8i).

     The $U(\psi_x^{'2} - \psi' \psi_{xx}')$ component appears to dominate the WAF signal for each of the three cases due to the similarity in
475   their spatial patterns (fig. 8g-i). To confirm this, all 4 terms of the WAF equation are shown as a bar graph in fig. 9d-f. When focusing on the first two components, which contribute to the x-component of the WAF equation, $U(\psi_x^{'2} - \psi' \psi_{xx}')$ dominates for each of the three cases. In contrast, the $U(\psi_x' \psi_y' - \psi' \psi_{xy}')$ component tends to be weaker. One reason for this occurrence is that in the second component of the WAF equation, ψ_{xy}' is associated with the divergence anomaly. It may be that, in the
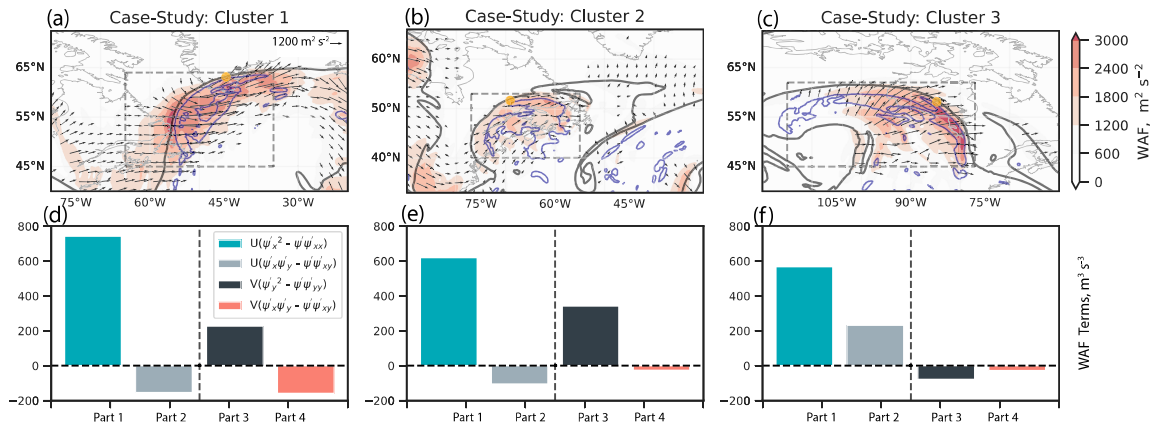
Figure 9. Evaluation of WAF. a-c shows the magnitude of WAF m^2 s^{-2} shaded in red and the direction of WAF propagation shown by the vectors. d-f shows a bar-chart in which the WAF equation is split into its four different components (Section 2.3, Equation 1) with units of m^3 s^{-3}. The $\frac{1}{|\overrightarrow{U}|}$ term at the start of the WAF equation is chosen to be excluded to more directly evaluate the importance of momentum transport and ageostrophic geopotential flux. The first two components are associated with the x-component of WAF. The last two components are associated with y-component WAF. The different components of WAF are computed within the dashed box domain from grid-points where the magnitude of WAF is in excess of 1200 m^2 s^{-2}.

cases selected, vorticity associated with NPV dominates the WAF signal over divergence. The y-component of WAF is weaker than the x-component for each case, which likely results from the meridional base-state wind (V) being weaker than the zonal base-state wind (U) when computing WAF. The $V(\psi_x'^2 - \psi'\psi_{yy}')$ term also dominates $V(\psi_x'\psi_y' - \psi'\psi_{xy}')$ in fig. 9e-f. However, fig. 9d does highlight the importance of case-to-case variability and that the influence of shear (linked to vorticity) and momentum transport may not always dominate the WAF signal during NPV-jet interactions.

To summarize, the three case-studies suggest that the presence of synoptic-scale NPV within a ridge (on the equatorward side of the jet stream) can be dynamically relevant for enhancing the instantaneous wave activity along the jet stream. The enhancement of wave activity can manifest from the increase in momentum transport and the anticyclonic shear in the vicinity of the jet that are attributed to result from the presence of synoptic-scale NPV. Given that these cases examine a single, instantaneous time-step of WAF, it is suspected that synoptic-scale NPV may be particularly relevant in enhancing wave activity in instances when multiple, synoptic-scale NPV features are present that exhibit temporal persistence.

4 Discussion

In this section, the results obtained are contextualized with respect to relevant literature on the PV perspective and NPV. Additionally, some limitations of the work are addressed. Through the dual use of a composite perspective and case-studies, it is
495 shown that NPV-jet interactions are consistently associated with an enhancement of kinetic energy along the mid-latitude jet stream. The composite perspective generalizes that NPV-jet interactions occur within ridge environments in which positive IVT anomalies are present on the westward flank of the ridge and are most frequent during Boreal Winter months over the Western Atlantic. Oertel et al. (2021) postulate that a pre-existing, strong jet stream is a conducive environment to favor the development of mesoscale NPV features. Winter months tend to be associated with the climatologically fastest jet stream winds (Iqbal et al.,
500 2018), hence the winter-time maximum in NPV-jet interactions may arise from the more favorable jet stream environment in elongating NPV features. Further evidence for this hypothesis (Oertel et al., 2021) is presented in fig. 4e-f in which despite the summer months having a 1.5 times greater area coverage in NPV of all sizes, synoptic-scale NPV was 10 times less likely to be observed compared to winter.

505 A caveat of this climatological analysis is that it is unique to the ERA5 dataset. It is noted that there is negligible impact on the climatology of NPV features when using a 0.25° resolution and interpolating to 0.5° resolution. When experimenting with temporally tracking NPV features with much finer grid-spacing such that PV structures within convective storms are more realistically resolved, the appearance of mesoscale NPV features becomes much more filamentary (Oertel and Schemm, 2021). As a result, different climatological results of NPV frequency may be obtained if the resolution of the dataset is sufficiently
510 high to produce more realistic and noisy PV structures. In experiments using the new CONUS404 dataset (Rasmussen et al., 2023), a 4 km resolution climatological dataset for the Continental US, it was observed that sub-mesoscale NPV features where much more frequent with respect to ERA5, but synoptic-scale NPV features were slightly less frequent.

The interaction of synoptic-scale NPV with the jet stream in the composite and case-study approach illustrates the interac-
515 tion between two opposing vorticity dipoles. Maximum values of jet stream wind speed anomalies are observed to be situated between the vorticity dipoles. Cunningham and Keyser (2004) use a barotropic framework to illustrate that the interaction of two dimensional vorticity dipoles can explain the development of jet streaks. This barotropic framework to explain jet streaks has also been applied to real-cases of synoptic-scale vorticity dipoles, such as trough-ridge couplet interactions (Pyle et al., 2004). In this research, the interaction of anticyclonic vorticity (NPV) with cyclonic vorticity on the poleward side of the jet
520 stream appears to also be conducive to strengthening of jet stream winds. Furthermore, the analysis presented here focuses on using a 2D framework, motivated by synoptic-scale NPV features predominantly being situated in the upper troposphere at about 250 - 300 hPa fig. A1. It is thus suspected that the 2D barotropic framework presented in Cunningham and Keyser (2004) may be useful to infer the role of synoptic-scale NPV in enhancing jet stream wind speeds. Additionally, the application of 2D vorticity inversions (Oertel and Schemm, 2021) on synoptic-scale NPV features may be appropriate if we assume that

525 synoptic-scale NPV can be generalized as 2D structures.

As discussed in Keller et al. (2019), two frameworks by which to understand the development of jet streaks is through PV advection by the irrotational wind or through the Cunningham and Keyser (2004) approach to define jet streaks via the interaction between two vorticity dipoles. In our composite analysis, strong irrotational wind fields were present in the clusters when

530 synoptic-scale NPV was located near the westward flank of the jet stream. This suggests that NPV can be embedded within the synoptic-scale divergent outflow and could contribute to the overall PV advection signal.

A caveat of the composite approach was that a contribution of NPV to the PV advection signal could not be adequately completed. Enhanced PV advection signals are expected when strong irrotational wind field anomalies develop within a large-

535 scale negative PV anomaly, such as within a ridge environment (Archambault et al., 2013). Hence, some of the wind speed signal could be attributed to the irrotational advection of low PV (but positive) air within the ridge environment that is diluted by vertical gradients of heating (Harvey et al., 2020). However, one of the NPV-jet event clusters identifies that synoptic-scale NPV can also frequently interact with the jet stream even when strong irrotational outflow is not present, such as along the eastern flank of a ridge (fig. 6i . This location is observed to have the same wind speed anomaly values as the other clusters

540 which have comparatively stronger irrotational wind fields. The result suggests that a strong irrotational wind field is not always necessary to obtain jet streaks. Jet streaks may potentially manifest through the remote advection of synoptic-scale NPV along the large-scale ridge environment.

As an additional point of clarification, care must also be taken in treating jet streaks associated with NPV-jet interactions as

545 2D, geostrophic features. While comparisons are made to the idealized jet streaks discussed in Cunningham and Keyser (2004), the composites here identify NPV-jet interactions to be frequently associated with highly ageostrophic environments (fig. 6g-i). Ageostrophy can significantly modify the sharpening of the PV gradient (Winters, 2021) and significantly contribute to altering the total wind speed profile. Hence, a more nuanced kinematic analysis of how NPV influences jet stream wind speeds is warranted.

550

Focusing on a dry vorticity perspective in combination with identifying NPV contours could provides a simple but appropriate framework for assessing the influence of NPV on the jet stream. A WAF approach was recently used to show that synoptic-scale NPV can degrade jet stream forecast skill within global numerical weather prediction models (Lojko et al., 2022). Specifically, it was found that the magnitude of the synoptic-scale NPV feature's anticyclonic vorticity was under-

555 represented and coincident with the manifestation of WAF errors. This finding is particularly interesting given that NPV-jet events appear to be geographically focused over the West Atlantic. Grazzini and Vitart (2015) show that Rossby wave packets initiated over the West Atlantic tend to be associated with poorer medium-range predictability over Europe. Our study shows that WAF packets (analogous to Rossby waves) tend to be emitted during NPV-jet interactions (fig. 6m-o) and that synoptic-scale NPV can be dynamically relevant in enhancing the magnitude of WAF (fig. 9a-f). It would thus be interesting to further

560   explore the relevance of synoptic-scale NPV for predictability within a composite perspective.

5   Conclusions

The study presents a composite overview on the climatology and dynamical impact of synoptic-scale bands of negative poten-
tial vorticity (NPV) on the West-North Atlantic jet stream. NPV features are identified using 6-hourly ERA5 data at 250 hPa

565   over the period 2000 - 2021. Using the PV field, values =<-0.01 PVU and >1650 km (>98th percentile) are used to identify
synoptic-scale NPV. 'Interactions' of NPV with the jet stream are identified when NPV features are located within 100 km of
a circumpolar 2 PVU contour. The 2 PVU contour is used to represent the jet stream and these interactions are referred to as
NPV-jet interactions.

570   The results are split into three parts: A climatological quantification of the frequency of NPV-jet interactions, a composite
analysis of the dynamics during NPV-jet interactions, and three case studies involving a mechanistic evaluation of synoptic-
scale NPV on the jet stream through the wave activity flux perspective. The climatological analysis shows that NPV-jet inter-
actions have a probability of occurring about 1.2 % of the time at particular grid-points over the Western Atlantic, maximized
at a latitude of 40°N. Interactions are most frequent during winter (> 2.5%) and least frequent during the summer months

575   (< 0.5%). The seasonal frequencies reaffirm previous case-study work (Harvey et al., 2020; Oertel et al., 2020) hypothesizing
that a pre-existing, strong jet stream (which is climatologically more likely to occur in winter) is an ideal environment in which
synoptic-scale NPV features can occur. The seasonal disparity in NPV-jet frequency may also arise due to convection during
winter months being predominantly coupled to the jet stream, while summer-time convection often arises without influence
from larger scale weather systems (Song et al., 2019).

580

An investigation of NPV trends in the study region illustrate an increasing trend over a narrow latitude band centered at
40°N encompassing Eastern North America and the Western Atlantic. For (all NPV) NPV-jet interactions, there has been a
relative frequency increase of over (45%) 11% in some localized regions of the Western Atlantic over the 22 year time-period
determined from linear trend analysis. This result bares similar resemblance to Lee et al. (2023) observation of increasing NPV

585   trend during Boreal Winter over the past four decades over the Western Atlantic. Albeit, the spatial extent and magnitude of the
trend in Lee et al. (2023) tend to be weaker than the percentages obtained in this work, perhaps indicating a recent enhancement
in the occrence of NPV over the West-Atlantic during the last two decades.

Generally, NPV-jet interactions are characterized by strong PV gradient anomalies (2.5 PVU per 100 km) which coincide

590   with enhanced (ageostrophic) wind speed anomalies exceeding 50 m s^{-1} (15 m s^{-1}). Even when NPV features are located
in regions far away from the diabatic heating that originally produced NPV, these positive anomalies persist, highlighting
that NPV can be associated with strengthened wind speeds without direct contribution from moist processes, which serves

to illustrate that synoptic-scale NPV features may be treated as predominantly dry, kinematic features. This assumption is complemented by case-studies that have observed elongated bands of NPV to advect quasi-adiabatically along the jet stream (Oertel et al., 2020; Lojko et al., 2022).

595

To gain additional insight on how NPV amplifies the jet stream, the 2D WAF equation at 250 hPa is applied. Composite analysis of the WAF denotes that a packet of WAF manifests at the time of NPV-jet interaction and subsequently propagates downstream. Further partitioning the WAF into its momentum and ageostrophic flux components through three archetype case-studies illustrates that strong momentum transport anomalies exist along the jet stream, adjacent to the NPV feature. Relative vorticity inversion can explain that the strong non-divergent wind circulation pattern manifests due to the interaction of the anticyclonic vorticity associated with NPV and enhanced cyclonic vorticity that lies along the poleward side of the jet stream. Additionally, the ageostrophic flux component of the WAF equation is maximized within NPV features when they are optimally embedded within a ridge environment (i.e., within a positive stream function anomaly). When NPV is present adjacent to the jet stream, the momentum terms and ageotrophic flux terms are observed to reinforce each other, contributing to localized maxima of the wave activity flux equation.

600

605

While large-scale features such as synoptic-scale cyclones are known to contribute substantially to the emission of wave activity (Orlanski and Katzfey, 1991; Takaya and Nakamura, 2001), NPV features can be associated with comparable magnitudes of wave activity. In a case-study by Lojko et al. (2022), the largest WAF errors within several global numerical weather prediction models did not manifest within cyclones, but within the synoptic-scale NPV feature. It was further shown that global numerical weather prediction models struggle with representing NPV features, as their anticyclonic circulation was comparatively weaker with respect to the reanalysis. Given that our study highlights that anticyclonic vorticity associated with NPV serves to enhance non-divergent winds and contribute to wave activity, the failure to resolve the magnitude of NPV's anticyclonic circulation in global weather models could lead to an under representation of kinetic energy along the jet stream.

610

615

Overall, our composite work reaffirms previous case-study observations that elongated NPV features can amplify jet stream winds and enhance the propagation of wave activity along the jet stream. Nevertheless, quantifying exactly by how much NPV amplifies the jet stream was not achieved through the analysis techniques used in this work. Designing a more elegant framework for quantifying the role of NPV on jet stream amplification would be a suitable next-step in constraining uncertainties associated with NPV-jet interactions. While a PV inversion may not be appropriate in quantifying the circulation in dynamically unstable regions of NPV, the application of a relative vorticity inversion (Oertel and Schemm, 2021) provides a suitable alternative. While the inversion can only be applied to the horizontal wind field at a single level, our work illustrates that synoptic-scale NPV features are predominantly confined to the upper-troposphere at approximately 250-300 hPa. This may permit the assumption to treat synoptic-scale NPV as quasi-2D structures.

620

625

More generally, there still remains plenty of mystery regarding the concept and properties of NPV. Why can synoptic-scale NPV persist for long periods of times and what are the processes by which NPV dissipates? Another interesting study would be to synthesize the full life-cycle of NPV from its suspected generation within convective-scale PV dipoles to its upscale growth

630   into an elongated filament of synoptic-scale NPV. Such research will further our understanding of the behaviour of NPV, which is pertinent to conduct given its suspected relevance in impinging on aviation turbulence (Trier and Sharman, 2016) and numerical weather prediction skill (Lojko et al., 2022).

Code and data availability. The Python based algorithm for identification of negative PV features and their interaction with the jet stream

635   can be downloaded from: https://github.com/AlexLojko/NPV_Algorithm. The Python script for computing a relative vorticity inversion can be downloaded from: https://github.com/evans36/miscellany. The ERA5 dataset is available from https://cds.climate.copernicus.eu/ which is downloaded using era5cli: https://github.com/eWaterCycle/era5cli

Appendix A: NPV-jet Interactions: Sensitivity Tests

This section illustrates the motivation for selecting the 250 hPa level and the 100 km distance threshold when defining NPV-

640   jet interactions. Figure A1 illustrates the identification of synoptic-scale NPV features for a selected year. NPV features are most frequent at 250 and 300 hPa for all length-scales of NPV. While the amount of NPV features is of the same order at each isobaric level when examining features smaller than 1000 km, the number of NPV features identified at 250 and 300 hPa are an order of magnitude more frequent when identifying NPV features greater than 1000 km. These results indicate that synoptic-scale NPV is predominantly an upper-tropospheric features, maximized at isobaric levels that are in close proximity

645   to the tropopause.

Figure B1a-c shows the characteristics of jet wind speeds during NPV-jet interactions at three different distance thresholds. Strong wind speed anomalies lie between two PV dipole anomalies for each threshold, resembling the theoretical work of Cunningham and Keyser (2004). When stronger wind speed maximum are present, for example, for the 0-100 km threshold,

650   the distance between the -0.5 PVU contour to the +0.5 PVU contour is shorter. In other words, the PV gradient between the positive PV anomaly with the negative PV anomaly is more compressed. At the 0-100 km threshold (fig. B1a), positive wind speed anomalies reaching 39 m s^{-1} are observed. Wind speeds decrease when the distance of synoptic-scale NPV feature to the jet stream decrease. At the 100-200 km threshold (fig. B1b), wind speed anomalies reach 33 m s^{-1} and 31 m s^{-1} in fig. B1c. While a statistical significance test is not performed, given that the 0-100 km threshold has a larger sample size of

655   events (n=4632) compared to the 100-200 km (n=2890) and 200-300 km (n=1949) thresholds, the strengthening of the wind speed appears to be a robust response as additional smoothing is expected to arise when computing the mean over more cases. While PV dipoles are observed for each threshold, the magnitude of the positive (negative) PV increases (decreases) with
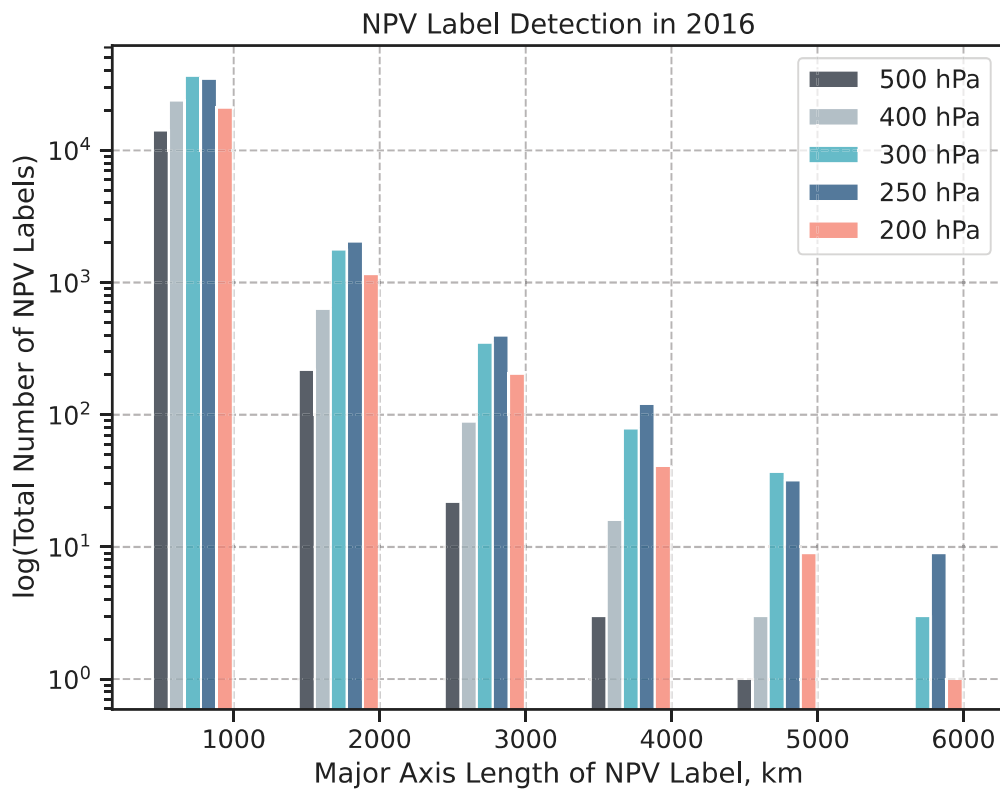
Figure A1. Frequency of NPV labels at different isobaric levels in 2016. The year 2016 is selected as it is associated with the most NPV-jet interactions at 250 hPa fig. 5d. The x-axis illustrates the major-axis length scale of NPV labels, binned at intervals of 1000 km. The y-axis shows the logged, total count of NPV labels.
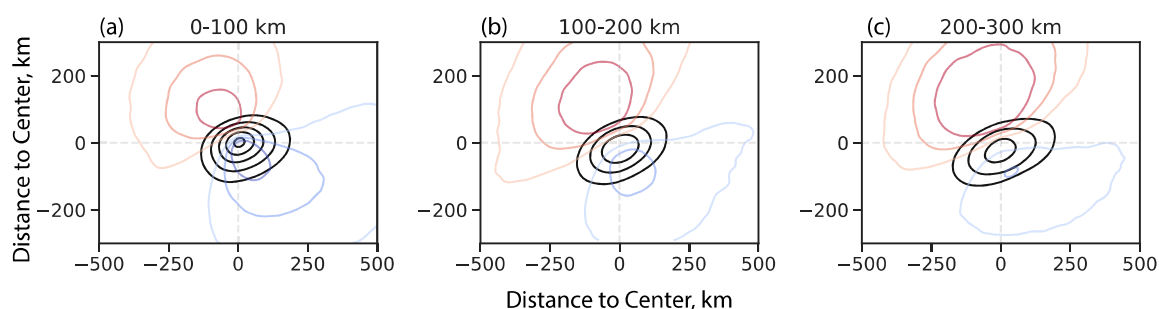
Figure B1. Wind speed composites centered on the interaction point at different NPV-jet distance thresholds: 0-100, 100-200 and 200-300 km. Note that the interaction point upon which centering is performed is defined differently in these set of plots. The 2 PVU coordinate that is in closest proximity to the NPV feature for each case is used as the interaction point. The choice to not center the composite on the NPV-jet interaction coordinate is made because wind speeds are expected to decrease with distance away from the 2 PVU contour (on the equatorward side of the jet stream). The x-axis and y-axis show the distance from the interaction point measured in km. Contours represent wind speeds at intervals of 4 m s^{-1} (22, 26, 30, 34, 38 m s^{-1}). PV anomaly contours are at intervals of 0.5 PVU (-1.5, -1, -0.5, 0.5, 1, 1.5 PVU).

distance from the 2 PVU contour. These changes may be artefacts arising from the centered composite analysis. For example, as NPV features move further away from the centroid, the negative PV anomaly field will become further smoothed out. It is 660 suspected that the strengthening of the positive PV anomaly may also be an artefact arising from the centered composite. These sensitivity tests motivate the selection of a narrow distance threshold criteria (in our study, using the 0-100 km threshold) for a more refined analysis in the main part of the manuscript.

Author contributions. AL designed the project, downloaded the data, performed the data analysis and wrote the manuscript. AW and AO 665 contributed to editing the manuscript. AW, AO and CJ worked on discussing the methodology with AL. All authors contributed to discussing the results.

Competing interests. The authors have no competing interests.

Acknowledgements. The research was conducted with grant support from the Momental Research Foundation and the National Center for Atmospheric Research Graduate Visitor Program Fellowship. Research visits to scientists at the Karlsruhe Institute of Technology and the

670   National Center for Atmospheric Research provided fruitful discussions on the project and the concept of negative potential vorticity. I also

      acknowledge help from Dr. Kevin Prince and Dr. Clark Evans regarding discussions on the relative vorticity inversion script.

References

Archambault, H. M., Bosart, L. F., Keyser, D., and Cordeira, J. M.: A climatological analysis of the extratropical flow response to recurving western North Pacific tropical cyclones, Monthly Weather Review, 141, 2325–2346, 2013.

675 Barnes, E. A., Hartmann, D. L., Frierson, D. M., and Kidston, J.: Effect of latitude on the persistence of eddy-driven jets, Geophysical research letters, 37, 2010.

Baumgart, M. and Riemer, M.: Processes governing the amplification of ensemble spread in a medium-range forecast with large forecast uncertainty, Quarterly Journal of the Royal Meteorological Society, 145, 3252–3270, 2019.

Berman, J. D. and Torn, R. D.: The impact of initial condition and warm conveyor belt forecast uncertainty on variability in the downstream

680 waveguide in an ECMWF case study, Monthly Weather Review, 147, 4071–4089, 2019.

Blanchard, N., Pantillon, F., Chaboureau, J.-P., and Delanoë, J.: Mid-level convection in a warm conveyor belt accelerates the jet stream, Weather and Climate Dynamics, 2, 37–53, 2021.

Bony, S., Stevens, B., Frierson, D. M., Jakob, C., Kageyama, M., Pincus, R., Shepherd, T. G., Sherwood, S. C., Siebesma, A. P., Sobel, A. H., et al.: Clouds, circulation and climate sensitivity, Nature Geoscience, 8, 261–268, 2015.

685 Braun, S. A. and Houze Jr, R. A.: The heat budget of a midlatitude squall line and implications for potential vorticity production, Journal of Atmospheric Sciences, 53, 1217–1240, 1996.

Ceppi, P., Brient, F., Zelinka, M. D., and Hartmann, D. L.: Cloud feedback mechanisms and their representation in global climate models, Wiley Interdisciplinary Reviews: Climate Change, 8, e465, 2017.

Chagnon, J. M. and Gray, S. L.: Horizontal potential vorticity dipoles on the convective storm scale, Quarterly Journal of the Royal Meteo-

690 rological Society: A journal of the atmospheric sciences, applied meteorology and physical oceanography, 135, 1392–1408, 2009.

Clarke, S. J., Gray, S. L., and Roberts, N. M.: Downstream influence of mesoscale convective systems. Part 1: influence on forecast evolution, Quarterly Journal of the Royal Meteorological Society, 145, 2933–2952, 2019.

Conzemius, R. J. and Montgomery, M. T.: Clarification on the generation of absolute and potential vorticity in mesoscale convective vortices, Atmospheric Chemistry and Physics, 9, 7591–7605, 2009.

695 Cunningham, P. and Keyser, D.: Dynamics of jet streaks in a stratified quasi-geostrophic atmosphere: Steady-state representations, Quarterly Journal of the Royal Meteorological Society: A journal of the atmospheric sciences, applied meteorology and physical oceanography, 130, 1579–1609, 2004.

Dacre, H. F., Martinez-Alvarado, O., and Mbengue, C. O.: Linking atmospheric rivers and warm conveyor belt airflows, Journal of Hydrometeorology, 20, 1183–1196, 2019.

700 Davis, C. A. and Emanuel, K. A.: Potential vorticity diagnostics of cyclogenesis, Monthly weather review, 119, 1929–1953, 1991.

Davis, C. A., Stoelinga, M. T., and Kuo, Y.-H.: The integrated effect of condensation in numerical simulations of extratropical cyclogenesis, Monthly Weather Review, 121, 2309–2330, 1993.

Dawson, A.: Windspharm: A high-level library for global wind field computations using spherical harmonics, Journal of Open Research Software, 4, 2016.

705 Grams, C. M. and Archambault, H. M.: The key role of diabatic outflow in amplifying the midlatitude flow: A representative case study of weather systems surrounding western North Pacific extratropical transition, Monthly Weather Review, 144, 3847–3869, 2016.

Grams, C. M., Magnusson, L., and Madonna, E.: An atmospheric dynamics perspective on the amplification and propagation of forecast error in numerical weather prediction models: A case study, Quarterly Journal of the Royal Meteorological Society, 144, 2577–2591, 2018.

710 Gray, S. L., Dunning, C., Methven, J., Masato, G., and Chagnon, J. M.: Systematic model forecast error in Rossby wave structure, Geophysical Research Letters, 41, 2979–2987, 2014.

Grazzini, F. and Vitart, F.: Atmospheric predictability and Rossby wave packets, Quarterly Journal of the Royal Meteorological Society, 141, 2793–2802, 2015.

Grazzini, F., Craig, G. C., Keil, C., Antolini, G., and Pavan, V.: Extreme precipitation events over northern Italy. Part I: A systematic classification with machine-learning techniques, Quarterly Journal of the Royal Meteorological Society, 146, 69–85, 2020.

715 Harvey, B., Methven, J., Sanchez, C., and Schäfler, A.: Diabatic generation of negative potential vorticity and its impact on the North Atlantic jet stream, Quarterly Journal of the Royal Meteorological Society, 146, 1477–1497, 2020.

Harvey, B. J., Methven, J., and Ambaum, M. H.: Rossby wave propagation on potential vorticity fronts with finite width, Journal of Fluid Mechanics, 794, 775–797, 2016.

Haynes, P. H. and McIntyre, M.: On the conservation and impermeability theorems for potential vorticity, Journal of Atmospheric Sciences,
720 47, 2021–2031, 1990.

Hersbach, H., Bell, B., Berrisford, P., Hirahara, S., Horányi, A., Muñoz-Sabater, J., Nicolas, J., Peubey, C., Radu, R., Schepers, D., et al.: The ERA5 global reanalysis, Quarterly Journal of the Royal Meteorological Society, 146, 1999–2049, 2020.

Hertenstein, R. F. and Schubert, W. H.: Potential vorticity anomalies associated with squall lines, Monthly weather review, 119, 1663–1672, 1991.

725 Hoskins, B.: A potential vorticity view of synoptic development, Meteorological Applications, 4, 325–334, 1997.

Iqbal, W., Leung, W.-N., and Hannachi, A.: Analysis of the variability of the North Atlantic eddy-driven jet stream in CMIP5, Climate Dynamics, 51, 235–247, 2018.

Keller, J. H., Grams, C. M., Riemer, M., Archambault, H. M., Bosart, L., Doyle, J. D., Evans, J. L., Galarneau, T. J., Griffin, K., Harr, P. A., et al.: The extratropical transition of tropical cyclones. Part II: Interaction with the midlatitude flow, downstream impacts, and implications
730 for predictability, Monthly Weather Review, 147, 1077–1106, 2019.

Lee, J. H., Kim, J.-H., Sharman, R. D., Kim, J., and Son, S.-W.: Climatology of clear-air turbulence in upper troposphere and lower stratosphere in the Northern Hemisphere using ERA5 reanalysis data, Journal of Geophysical Research: Atmospheres, 128, e2022JD037 679, 2023.

Li, J., Feng, Z., Qian, Y., and Leung, L. R.: A high-resolution unified observational data product of mesoscale convective systems and isolated
735 deep convection in the United States for 2004–2017, Earth System Science Data Discussions, 2020, 1–48, 2020.

Lojko, A., Payne, A., and Jablonowski, C.: The Remote Role of North-American Mesoscale Convective Systems on the Forecast of a Rossby Wave Packet: A Multi-Model Ensemble Case-Study, Journal of Geophysical Research: Atmospheres, 127, e2022JD037 171, 2022.

Lorenz, D. J. and Hartmann, D. L.: Eddy–zonal flow feedback in the Northern Hemisphere winter, Journal of climate, 16, 1212–1227, 2003.

Madonna, E., Wernli, H., Joos, H., and Martius, O.: Warm conveyor belts in the ERA-Interim dataset (1979–2010). Part I: Climatology and
740 potential vorticity evolution, Journal of climate, 27, 3–26, 2014.

Martin, J. E.: Quasi-geostrophic diagnosis of the influence of vorticity advection on the development of upper level jet-front systems, Quarterly Journal of the Royal Meteorological Society, 140, 2658–2671, 2014.

Minobe, S., Kuwano-Yoshida, A., Komori, N., Xie, S.-P., and Small, R. J.: Influence of the Gulf Stream on the troposphere, Nature, 452, 206–209, 2008.

745 Oertel, A. and Schemm, S.: Quantifying the circulation induced by convective clouds in kilometer-scale simulations, Quarterly Journal of the Royal Meteorological Society, 147, 1752–1766, 2021.

Oertel, A., Boettcher, M., Joos, H., Sprenger, M., and Wernli, H.: Potential vorticity structure of embedded convection in a warm conveyor belt and its relevance for large-scale dynamics, Weather and Climate Dynamics, 1, 127–153, 2020.

Oertel, A., Sprenger, M., Joos, H., Boettcher, M., Konow, H., Hagen, M., and Wernli, H.: Observations and simulation of intense convection embedded in a warm conveyor belt–how ambient vertical wind shear determines the dynamical impact, Weather and Climate Dynamics, 2, 89–110, 2021.

Orlanski, I. and Katzfey, J.: The life cycle of a cyclone wave in the Southern Hemisphere. Part I: Eddy energy budget, Journal of Atmospheric Sciences, 48, 1972–1998, 1991.

Pfahl, S., Schwierz, C., Croci-Maspoli, M., Grams, C. M., and Wernli, H.: Importance of latent heat release in ascending air streams for atmospheric blocking, Nature Geoscience, 8, 610–614, 2015.

Prosser, M. C., Williams, P. D., Marlton, G. J., and Harrison, R. G.: Evidence for Large Increases in Clear-Air Turbulence Over the Past Four Decades, Geophysical Research Letters, 50, e2023GL103 814, 2023.

Pyle, M. E., Keyser, D., and Bosart, L. F.: A diagnostic study of jet streaks: Kinematic signatures and relationship to coherent tropopause disturbances, Monthly weather review, 132, 297–319, 2004.

Rasmussen, R., Chen, F., Liu, C., Ikeda, K., Prein, A., Kim, J., Schneider, T., Dai, A., Gochis, D., Dugger, A., et al.: CONUS404: The NCAR-USGS 4-km long-term regional hydroclimate reanalysis over the CONUS, Bulletin of the American Meteorological Society, 2023.

Rodwell, M. J., Magnusson, L., Bauer, P., Bechtold, P., Bonavita, M., Cardinali, C., Diamantakis, M., Earnshaw, P., Garcia-Mendez, A., Isaksen, L., et al.: Characteristics of occasional poor medium-range weather forecasts for Europe, Bulletin of the American Meteorological Society, 94, 1393–1405, 2013.

Röthlisberger, M., Martius, O., and Wernli, H.: Northern Hemisphere Rossby wave initiation events on the extratropical jet—A climatological analysis, Journal of Climate, 31, 743–760, 2018.

Rowe, S. M. and Hitchman, M. H.: On the relationship between inertial instability, poleward momentum surges, and jet intensifications near midlatitude cyclones, Journal of the Atmospheric Sciences, 73, 2299–2315, 2016.

Song, F., Feng, Z., Leung, L. R., Houze Jr, R. A., Wang, J., Hardin, J., and Homeyer, C. R.: Contrasting spring and summer large-scale environments associated with mesoscale convective systems over the US Great Plains, Journal of Climate, 32, 6749–6767, 2019.

Spreitzer, E., Attinger, R., Boettcher, M., Forbes, R., Wernli, H., and Joos, H.: Modification of potential vorticity near the tropopause by nonconservative processes in the ECMWF model, Journal of the atmospheric sciences, 76, 1709–1726, 2019.

Steinfeld, D. and Pfahl, S.: The role of latent heating in atmospheric blocking dynamics: a global climatology, Climate Dynamics, 53, 6159–6180, 2019.

Takaya, K. and Nakamura, H.: A formulation of a phase-independent wave-activity flux for stationary and migratory quasigeostrophic eddies on a zonally varying basic flow, Journal of the Atmospheric Sciences, 58, 608–627, 2001.

Thompson, C. F., Schultz, D. M., and Vaughan, G.: A global climatology of tropospheric inertial instability, Journal of the Atmospheric Sciences, 75, 805–825, 2018.

Trier, S. B. and Sharman, R. D.: Mechanisms influencing cirrus banding and aviation turbulence near a convectively enhanced upper-level jet stream, Monthly Weather Review, 144, 3003–3027, 2016.

Weijenborg, C., Friederichs, P., and Hense, A.: Organisation of potential vorticity on the mesoscale during deep moist convection, Tellus A: Dynamic Meteorology and Oceanography, 67, 25 705, 2015.

Weijenborg, C., Chagnon, J., Friederichs, P., Gray, S., and Hense, A.: Coherent evolution of potential vorticity anomalies associated with deep moist convection, Quarterly Journal of the Royal Meteorological Society, 143, 1254–1267, 2017.

785 Wernli, H. and Davies, H. C.: A Lagrangian-based analysis of extratropical cyclones. I: The method and some applications, Quarterly Journal of the Royal Meteorological Society, 123, 467–489, 1997.

Wilks, D.: "The stippling shows statistically significant grid points": How research results are routinely overstated and overinterpreted, and what to do about it, Bulletin of the American Meteorological Society, 97, 2263–2273, 2016.

Winters, A. C.: Kinematic processes contributing to the intensification of anomalously strong North Atlantic jets, Quarterly Journal of the
790 Royal Meteorological Society, 147, 2506–2532, 2021.

Woollings, T., Papritz, L., Mbengue, C., and Spengler, T.: Diabatic heating and jet stream shifts: A case study of the 2010 negative North Atlantic Oscillation winter, Geophysical Research Letters, 43, 9994–10, 2016.